CLASH-VLT: constraints on $f(R)$ gravity models with galaxy clusters using lensing and kinematic analyses

L. Pizzuti,[1] **B. Sartoris,**[1,2] **L. Amendola,**[4] **S. Borgani,**[1,2,3] **A. Biviano,**[2] **K. Umetsu,**[5] **A. Mercurio,**[6] **P. Rosati,**[7] **I. Balestra,**[2] **G. B. Caminha,**[7] **M. Girardi,**[1,2] **C. Grillo,**[7] **M. Nonino.**[2]

[1]Dipartimento di Fisica, Sezione di Astronomia, Università di Trieste,
 Via Tiepolo 11, I-34143 Trieste, Italy

[2]INAF - Osservatorio Astronomico di Trieste,
 Via Tiepolo 11, I-34143 Trieste, Italy

[3]INFN - Sezione di Trieste,
 Via Valerio 2, I-34127 Trieste, Italy

[4]Institut für Theoretische Physik, Universität Heidelberg,
 Philosophenweg 16, D-69120 Heidelberg, Germany

[5]5 Institute of Astronomy and Astrophysics, Academia Sinica, P.O. Box 23-141,
 Taipei 10617, Taiwan

[6]Osservatorio Astronomico di Capodimonte,
 Via Moiariello 16, I-80131 Napoli, Italy

[7]Dipartimento di Fisica e Scienze della Terra, Università di Ferrara,
 Via Saragat 1, I-44122 Ferrara, Italy

E-mail: pizzuti@oats.inaf.it

Abstract. We perform a maximum likelihood kinematic analysis of the two dynamically relaxed galaxy clusters MACS J1206.2-0847 at $z = 0.44$ and RXC J2248.7-4431 at $z = 0.35$ to determine the total mass profile in modified gravity models, using a modified version of the MAMPOSSt code of Mamon, Biviano and Boué. Our work is based on the kinematic and lensing mass profiles derived using the data from the Cluster Lensing And Supernova survey with Hubble (hereafter CLASH) and the spectroscopic follow-up with the Very Large Telescope (hereafter CLASH-VLT). We assume a spherical Navarro-Frenk-White (NFW hereafter) profile in order to obtain a constraint on the fifth force interaction range λ for models in which the dependence of this parameter on the enviroment is negligible at the scale considered (i.e. $\lambda = const$) and fixing the fifth force strength to the value predicted in $f(R)$ gravity. We then use information from lensing analysis to put a prior on the other NFW free parameters. In the case of MACSJ 1206 the joint kinematic+lensing analysis leads to an upper limit on the effective interaction range $\lambda \leq 1.61\,\mathrm{Mpc}$ at $\Delta\chi^2 = 2.71$ on the marginalized distribution. For RXJ 2248 instead a possible tension with the ΛCDM model appears when adding lensing information, with a lower limit $\lambda \geq 0.14\,\mathrm{Mpc}$ at $\Delta\chi^2 = 2.71$. This is consequence of the slight difference between the lensing and kinematic data, appearing in GR for this cluster, that could in principle be explained in terms of modifications of gravity. We discuss the impact of systematics and the limits of our analysis as well as future improvements of the results obtained. This work has interesting implications in view of upcoming and future large imaging and spectroscopic surveys, that will deliver lensing and kinematic mass reconstruction for a large number of galaxy clusters.

Contents

1 Introduction

The discovery of the late-time accelerated expansion of the Universe (refs. [1, 2]) at the turn of the XX century has posed one of the most challenging problems in modern physics. The current cosmological concordance model, or ΛCDM model, correctly predicts the observed expansion history but requires the introduction of a cosmological constant Λ, an additional term in the Einstein equations that has no natural explanation in the framework of standard physics. In the last decade several alternatives have been proposed to explain the origin of the acceleration; a possible solution is to modify the theory of General Relativity (GR hereafter) on large scales by introducing new degrees of freedom which can reproduce the same effect of a cosmological constant (see e.g. refs. [3, 4]) and at the same time propagate a new force. Even when considering theories where the predicted expansion history is identical to that of the ΛCDM model, the evolution of the perturbations can be significantly different from ΛCDM.

General departures from GR change the relations between the gravitational potentials Φ and Ψ in the linearly perturbed Friedmann-Lemaitre-Robertson-Walker metric and the fluctuations of the matter density field both at linear and non-linear level (ref. [5]). We can generally parametrize these deviations in terms of two dimensionless functions $\eta(k, a)$, $Y(k, a)$ (see e.g. ref. [6]) or their combination, which can be constrained with a broad range of observational probes, such as Cosmic Microwave Background anisotropies (refs. [7–9]), Barionic Acoustic Oscillations (e.g. ref. [10]), redshift space distortions (e.g. ref. [6, 11]), galaxy clusters (e.g. refs. [12–14]). In particular, the analysis of ref. [9], further confirmed by ref. [15], seems to indicate a tension in the amount of clustering with the concordance model when CMB data are combined with low-redshift probes (galaxy weak lensing and redshift space distortions) that could be explained in terms of modified gravity.

Since GR is tested at high precision at Solar System scales (see e.g. ref. [16] and references therein), modified gravity (hereafter MG) models must match the standard theory of gravity in this regime. Solar System constraints on modification of gravity ca be accounted

for a screening mechanism which suppresses the modifications restoring GR in high density enviroments (see e.g. ref [17] for a review). Alternatively, local gravity constraints can be escaped by assuming that baryons are decoupled (ref. [18]).

Among the modified gravity models, a very large class is represented by the Horndeski lagrangian (ref. [19]), the most general theory of massless gravity and a single scalar field with second-order equations of motion. In the quasi-static regime, i.e. when the wave nature of the scalar degree of freedom can be neglected, the extra force carried by the scalar field manifests itself as a Yukawa correction to the Newtonian potential, characterized by two parameters, a strength Q and a range λ. Aim of this paper is to constrain these parameters by employing reconstruction of the mass profiles of galaxy clusters with kinematic analysis and strong+weak lensing analysis. To simplify our task we apply the method to a sub-class of Horndeski models, the so-called $f(R)$ models, in which case it turns out that $2Q^2 = 1/3$ and also that the lensing dynamics is not distorted. In these models the role of the additional degree of freedom is played by $f_{,R} = df/dR$ that acts as a scalar field with a characteristic mass $m_{f_R} = 1/\lambda$. The new force is suppressed in high density regions by a non-linear mechanism that quenches deviations from GR, as required by consistency with the current observations, known as chameleon screening (ref. [20]).

We aim then at constraining the interaction range λ by performing a joint kinematics and lensing analysis of the galaxy clusters, MACS J1206.2-0847 (hereafter MACS 1206) at redshift $z = 0.44$ and RXC J2248.7-4431 (hereafter RXJ 2248) at $z = 0.35$, which have been analysed in detail as part of the Cluster Lensing And Supernova survey with Hubble (CLASH, ref. [21]) and the spectroscopic follow-up with the Very Large Telescope (CLASH-VLT, ref. [22]) programs. We determine the dynamic mass profiles in $f(R)$ gravity under the assumptions of spherical symmetry and dynamical relaxation of the clusters by using the *MAMPOSSt* code of ref. [23], in which we included a parametric expression of the gravitational potential valid for generic MG models. This expression is obtained by imposing a NFW profile (ref. [24]) for the matter density perturbation. With a Maximum Likelihood approach we constrain the free parameters in our analysis, namely the scale radius r_s, the radius r_{200} (a proxy for the virial radius), the parameter describing the velocity anisotropy profile $\beta(r)$ and the interaction range λ. We assume a constant value for the scalaron mass $m_{f_R} = 1/\lambda$, which means we are neglecting the change in m_{f_R} due to the environmental density. This can be translated as dealing with models where the screening mechanism takes place at scales much smaller than the cluster size (e.g. few kpc), but also with models for which the screening is so effective that maintains the field mass nearly constant to the value inside the overdensity. In this case, the results we obtain on λ refer to an effective "screened" $f_{,R}$, which is much smaller than the background field (ref. [25]). We further combine the *MAMPOSSt* Likelihood with the posterior probability distribution of the NFW parameters r_s and r_{200} obtained by the joint strong+weak lensing analysis of ref. [26] in order to improve our results on λ.

The paper is organized as follows: in Sect. 2 we discuss the general parametrization of the metric potentials in modified gravity, the application on the $f(R)$ class of MG models. In Sect 3 we present the *MAMPOSSt* method and the modifications we made to the code. Sect. 4 is dedicated to describe the properties of the two analysed galaxy clusters. In Sect. 5 we show our results, which are further discussed in Sect. 6, where we also draw our main conclusions. Throughout this paper we assume a flat ΛCDM universe with $\Omega_m = 0.3$ for the matter density parameter and $H_0 = 70$ km s^{-1}Mpc^{-1} for the present-day Hubble constant to convert observed angular scales into physical scales.

2 Theoretical framework

2.1 General parametrization

The spacetime structure of a galaxy cluster is well described by a linear perturbation of the Friedmann Lemaitre Robertson Walker (FLRW hereafter) metric, which in spherical coordinates is given by:

$$ds^2 = a^2(\tau) \left\{ \left(1 + 2\frac{\Phi}{c^2}\right) d\tau^2 - \left(1 - 2\frac{\Psi}{c^2}\right) [d\chi^2 + f_K^2(\chi)d\Omega^2] \right\}, \tag{2.1}$$

where we adopted the conformal Newtonian gauge choice (see ref. [27]). Although we assume $\Phi, \Psi \ll 1$, we do not restrict the value of the matter perturbations. Φ and Ψ are the scalar Bardeen potentials defined in ref. [28], $a(\tau)$ is the expansion factor, which is a function of the conformal time τ. $f_K(\chi)$ is a function of the curvature K and the radial comoving coordinate χ, with $f_K(\chi) = \chi$ for a flat background universe with $K = 0$.

In General Relativity $\Phi = \Psi \equiv \Phi_N$, where Φ_N is the usual Newtonian potential obeying the Poisson equation (in Fourier space):

$$k^2\Phi_N = -\frac{3}{2}\Omega_m(t)\delta_m H^2. \tag{2.2}$$

In the expression above $k = k_{com}/a$ is the physical wavenumber, $\Omega_m(t)$ is the time dependent matter density parameter, H is the Hubble parameter, $\delta_m = (\rho_m - \rho_{bg})/\rho_{bg}$ the matter density constrast, where ρ_{bg} is the background matter density at that time. Here we have already assumed spherical symmetry, i.e. $\Phi_N = \Phi_N(k)$, $\delta_m = \delta_m(k)$. In a general modifed gravity scenario, Φ is no longer equal to Ψ, and the Poisson equation should be changed as (see e.g. refs. [29], [30]):

$$k^2\Phi = -\frac{3}{2}Y(k,a)\Omega_m(t)\delta_m H^2, \tag{2.3}$$

$$k^2(\Phi + \Psi) = -\frac{3}{2}Y(k,a)[1 + \eta(k,a)]\Omega_m(t)\delta_m H^2. \tag{2.4}$$

Here $Y(k,a)$ is the effective gravitational constant and $\eta(k,a) = \Psi/\Phi$ is the anisotropic stress, both equal to unity in standard gravity. As shown in ref. [29], we can write these quantities in terms of five parameters introduced in ref. [30]:

$$Y(k,a) = h_1\left(\frac{1 + k^2 h_5}{1 + k^2 h_3}\right), \qquad\qquad \eta(k,a) = h_2\left(\frac{1 + k^2 h_4}{1 + k^2 h_5}\right). \tag{2.5}$$

Here, $h_1 ... h_5$ are functions of time only and can be considered constant for small redshift ranges, as the one spanned by our clusters. It's useful to define $Q^2 = (h_5 - h_3)/2h_3$ and $\hat{Q}^2 = (h_4 - h_3)/2h_3$ such that:

$$Y\eta = h_1 h_2\left(1 + \frac{2\hat{Q}^2 k^2}{m^2 + k^2}\right), \qquad\qquad Y = h_1\left(1 + \frac{2Q^2 k^2}{m^2 + k^2}\right), \tag{2.6}$$

which are in the form of Yukawa potentials with strength $\hat{Q}^2$ and Q^2 respectively and characteristic mass $m^2 = 1/h_3$. Scale-independent standard gravity is recovered for $m \to \infty$ and $h_1, h_2 \to 1$.

Inserting the Navarro-Frenk-White density profile of ref. [31] in the RHS of (2.3) and taking the anti-Fourier transform, the expression for the time-time Bardeen potential in real space could be written as

$$\Phi(r) = h_1 \left[G \int_{r_0}^{r} \frac{dx}{x^2} M(x) + 2Q^2 \phi_{mg}(r) \right]. \tag{2.7}$$

The first term in eq. (2.7) is the Newtonian potential Φ_N; inside the integral, $M(x)$ is the standard-gravity NFW mass profile:

$$M(r) = M_{200} \left[\log(1 + r/r_s) - r/r_s(1 + r/r_s)^{-1} \right] \times \left[\log(1 + c) - c/(1 + c) \right]^{-1}, \tag{2.8}$$

described by the scale radius r_s and the parameter r_{200} which is the radius of a sphere enclosing an overdensity 200 times the critical density at the cluster redshift; M_{200} is the mass at r_{200} and $c = r_{200}/r_s$ is the concentration. The second term includes the contribution of GR departures and it is given by:

$$\phi_{mg}(r) = \frac{2\pi G \rho_0}{r} r_s^3 \left\{ e^{-m(r_s+r)} \left[\text{Ei}(m\,r_s) - \text{Ei}(m(r_s + r)) \right] \right.$$

$$\left. - e^{-m(r_s+r)} \text{Ei} \left[-m(r_s + r) \right] + e^{m(r_s-r)} \text{Ei}(-m\,r_s) \right\}, \tag{2.9}$$

where ρ_0 is the normalization of the NFW density profile and is a function of the parameters r_s, r_{200}; m is the characteristic mass defined above. As $m \to 0$, it can be shown numerically that the additional contribution $\phi_{mg}(r)$ tends to be equal to $\Phi_N(r)$ for a given r.

Combining eq. (2.3) and eq. (2.4), we obtain a similar expression for the space-space potential Ψ:

$$\Psi(r) = h_1 h_2 \left[G \int_{r_0}^{r} \frac{dx}{x^2} M(x) + 2\hat{Q}^2 \phi_{mg}(r) \right]. \tag{2.10}$$

The effect of modifications of gravity is thus completely determined by the choice of the parameters $h_1, h_2, Q, \hat{Q}, m$. In the general case they are totally independent from each other, but, as we will see in the next paragraph, fixing a particular model allows us to establish relations among these parameters, reducing the number of degrees of freedom.

Since in a galaxy cluster the typical velocities of the galaxies are non-relativistic ($\sim 10^3\,km/s << c$), in the weak field limit the motion of the galaxies is determined only by the time-time component of the metric. As follows from the geodesics equation, the acceleration experienced by a non-relativistic particle is sourced by the gradient of Φ:

$$\frac{d^2 \vec{x}}{dt^2} = -\nabla \Phi. \tag{2.11}$$

It is thus possible to infer the Bardeen potential Φ by the dynamical analysis of the observed galaxies in a cluster. The combination of Ψ and Φ can instead be determined through gravitational lensing observations. Indeed, photons perceive the gravitational potential due to the contribution of both time-time and space-space metric components. As in ref. [13], we define at leading order in Ψ, Φ a lensing potential $\Phi_{lens} = (\Psi + \Phi)/2$, which is related to the lensing mass density profile through the Poisson equation

$$\nabla^2 \Phi_{lens} = 4\pi G \rho_{lens}. \tag{2.12}$$

Hence, gravitational lensing analysis of a galaxy cluster gives the sum of the Bardeen potentials plus negligible corrections.

2.2 $f(R)$ gravity

One of the simplest and most investigated alternatives to General Relativity (GR) is the class of scalar-tensor theories known as $f(R)$ gravity proposed by ref. [32], in which the Einstein-Hilbert action is modified by adding a general non-linear function of the Ricci curvature scalar R. In the Jordan frame the total action (in units $c = 1$) reads:

$$S = \frac{1}{16\pi G} \int \sqrt{-g}[R + f(R)]d^4x + S_m[\Psi_m, g_{\mu\nu}], \qquad (2.13)$$

where S_m is the action of the matter field Ψ_m. Note that for $f(R) = \text{const} \equiv -2\Lambda$ we recover GR in presence of a cosmological constant.

Variation of eq. (2.13) with respect to the metric $g_{\mu\nu}$ gives rise to the modifed Einstein equations:

$$(1 + f_{,R})R_{\mu\nu} - \frac{1}{2}g_{\mu\nu}[f(R) + R] + (g_{\mu\nu}\Box - \nabla_\mu\nabla_\nu)f_{,R} = 8\pi G T_{\mu\nu}. \qquad (2.14)$$

The quantity

$$f_{,R} = \frac{df(R)}{dR},$$

usually known as the scalaron, is a new degree of freedom which can be interpreted as a scalar field, mediating an additional fifth force with a characteristic range described by the physical Compton length λ (see below).

In the case of flat FLRW universe, the Ricci scalar is given by

$$R_b = 6\left(\frac{\ddot{a}}{a} + H^2\right) = 3H_0^2\Omega_m\left[(1+z)^3 + 4\frac{\Omega_\Lambda}{\Omega_m}\right], \qquad (2.15)$$

where the subscript b indicates background value, $a(t)$ is the scale factor, Ω_m is the matter density parameter today, and $H = \dot{a}(t)/a(t)$ is the Hubble parameter; overdot means derivative with respect to the cosmic time t. Under the assumption of the cosmological principle, from eq. (2.14) we can further derive the Friedmann equation:

$$H^2 + \frac{1}{6}f(R) - \frac{\ddot{a}}{a}f_{,R} + H\dot{f}_{,R} = \frac{8\pi G}{3}\rho_{m,b}. \qquad (2.16)$$

The trace of eq. (2.14) shows explicity the role of the field $f_{,R}$. Indeed we have:

$$\Box f_{,R} = \frac{1}{3}\left[R - f_{,R}R + 2f(R) - 8\pi G\rho_m\right], \qquad (2.17)$$

which could be seen as the equation of motion for the scalaron, with a canonical kinetic term and an effective potential

$$\frac{\partial V_{eff}}{\partial f_{,R}} = \frac{1}{3}\left[R - f_{,R}R + 2f(R) - 8\pi G\rho_m\right]. \qquad (2.18)$$

For the class of viable models that in the high-curvature regime satisfy $|f_{,R}| \ll 1$ and $|f(R)/R| \ll 1$ (see e.g. refs. [33, 34]), V_{eff} has an extremum at the general-relativistic value

$$R = \frac{8\pi G}{3}\rho_m.$$

The concavity of the potential in the extremum is given by its second derivative:

$$m_{f_R}^2 \equiv \frac{\partial^2 V_{eff}}{\partial f_{,R}^2} = \frac{1}{3} \left(\frac{1 + f_{,R}}{f_{,RR}} - R \right), \tag{2.19}$$

where $f_{,RR} = df_{,R}/dR$; m_{f_R} represents the scalaron mass and its inverse $\lambda = 1/m_{f_R}$, the Compton length, gives the typical interaction range of the fifth force. In the limit of $|Rf_{,RR}|, |f_{,R}| \ll 1$ one has

$$m_{f_R}^2 \sim \frac{1}{3f_{,RR}} \tag{2.20}$$

Constraining the scalaron mass means therefore to constrain the second derivative of $f(R)$, rather than just $f_{,R}$. Notice also that, in this approximation, in order to have a stable minimum, $f_{,RR} \geq 0$ is thus required. Ref. [35] argued that this is a critical constraint to avoid short timescale instabilities in the high curvature regime. Physically the condition means a non-tachyonic scalaron field.

Looking to perturbations in the FRW background, under the quasi-static approximation for which $\nabla f_{,R} \gg \dot{f}_{,R}$ (which is achieved for scales $k/aH \gg 1$), it is possibile to rearrange the field equation (2.17) in a Poisson-like form for the fluctuations, as shown in [36]:

$$\nabla^2 \delta f_{,R} = \frac{1}{3} \delta R(f_{,R}) - \frac{8}{3} \pi G \delta \rho_m, \tag{2.21}$$

where we are working in physical coordinates and the perturbed quantities are defined as $\delta X = X - X_b$. Solving the linearized modified Einstein equations in the Newtonian gauge of eq. (2.1) we can furthermore derive the Poisson equation for the Bardeen potential Φ:

$$\nabla^2 \Phi = \frac{16\pi G}{3} \delta \rho_m - \frac{1}{6} \delta R(f_{,R}). \tag{2.22}$$

In the linear regime, the curvature perturbations are everywhere small compared to the GR value $\delta R \ll 8\pi G \delta \rho_m$. This happens for example if $|f_{,R(b)}| \gg |\Phi_N|$, where $\Phi_N \sim 10^{-5}$ is the typical Newtonian potential for a galaxy cluster. Following e.g. [33] and references therein we can expand the fluctuations as:

$$\delta R \simeq \left(\frac{\partial R}{\partial f_{,R}} \right)_{R_b} \delta f_{,R} = 3\bar{m}_{f_R}^2 \delta f_{,R}, \tag{2.23}$$

where $\bar{m}_{f_R}^2$ refers to the background scalaron mass. Combining the last three equations and writing the result in Fourier space, we obtain an expression for the time-time Bardeen potential:

$$\Phi = -\frac{4\pi G \delta \rho_m}{1 + f_{,R}} \frac{1}{k^2} \left(1 + \frac{1}{3} \frac{k^2}{\bar{m}_{f_R}^2 + k^2} \right), \tag{2.24}$$

which is the same as eq. (2.3) expliciting $Y(k, a)$ with the assumption:

$$2Q^2 = 1/3, \quad h_1 = (1 + f_{,R})^{-1} \simeq 1, \quad m = \bar{m}_{f_R}. \tag{2.25}$$

A similar equation can be derived for Ψ:

$$\Psi = -h_1 h_2 \frac{4\pi G \delta \rho_m}{k^2} \left(1 - 2\hat{Q}^2 \frac{k^2}{\bar{m}_{f_R}^2 + k^2} \right) = -\frac{4\pi G \delta \rho_m}{1 + f_{,R}} \frac{1}{k^2} \left(1 - \frac{1}{3} \frac{k^2}{\bar{m}_{f_R}^2 + k^2} \right), \tag{2.26}$$

where $2\hat{Q}^2 = -1/3$, $h_2 = 1$. In real space, for a NFW mass density profile, we finally get:

$$\Phi(r) = \left[G \int_{r_0}^{r} \frac{dx}{x^2} M(x) + \frac{1}{3}\phi_{mg}(r, \bar{m}_{f_R}) \right] + O(f_{,R}); \qquad (2.27)$$

$$\Psi(r) = \left[G \int_{r_0}^{r} \frac{dx}{x^2} M(x) - \frac{1}{3}\phi_{mg}(r, \bar{m}_{f_R}) \right] + O(f_{,R}). \qquad (2.28)$$

We are now left with only one free parameter, i.e. the background scalaron mass $\bar{m}_{f_R}$ (or, equivalently, the interaction range λ), related to the background $f_{,R}$ through eq. (2.19). The maximum enhancement of gravity due to the effect of the fifth force is $1/3$ with respect to GR on scales $k \gg \bar{m}_{f_R}$. Equation (2.27) is what we are going to use in the analysis of the cluster dynamics in order to constrain $\lambda = 1/m$.

It is straightforward to compute the lensing potential form eqs. (2.27), (2.28):

$$\Phi_{lens}(r) = \frac{1}{2}(\Phi + \Psi) = G \int_{r_0}^{r} \frac{dx}{x^2} M(x) + O(f_{,R}). \qquad (2.29)$$

In $f(R)$ models photons perceive only the Newtonian part of gravity except for a correction of order $\sim f_{,R}$. Thus, for models with $|f_{,R}| \ll 1$, geodesics of photons are unchanged by the presence of the new degree of freedom. This feature is physically related to the property that $f(R)$ and scalar-tensor theories can be generated by a conformal rescaling of the metric, together with the conformal invariance of electromagnetism (see e.g. [37]).

For small field values $|f_{,R(b)}| \ll |\Phi_N|$, the characteristic mass becomes larger and the contribution of the force modification is suppressed. Moreover, if we consider an overdensity such as a galaxy cluster (assumed to be spherically simmetric), in the interior the field is close the minimum of the effective potential, given by the GR limit $\delta R \simeq 8\pi G \delta \rho_m$; in this case field gradients are negligible except for a shell at the boundary where the overdensity matches the cosmological background. The thickness of this shell is given by

$$\Delta r = r_{match} - S. \qquad (2.30)$$

In the above equation, r_{match} indicates the boundary of the overdensity and S is dubbed the *screening radius*. For $r < S$ gravity is described by standard GR and eq. (2.22) becomes the usual Poisson equation for the Newtonian potential.

In order to use the same formalism of eq. (2.24), derived by linearizing the curvature perturbations, inside the overdensity, we have to replace $\bar{m}_{f_R}$ with an effective mass $m_{eff}(k)$, which depends on the environmental density, and is related to the scalaron minimum value inside the overdensity. If in the region enclosed within the screening radius S we have full screening, m_{eff} becomes so large that the field does not propagate and the additional terms in eqs. (2.24),(2.28) tend to zero. The mechanism to recover GR in high density regions by using an enviroment-dependent field is known as the chameleon mechanism (ref. [20]).

Assuming a constant value for m_{eff} in this picture (i.e. neglecting the dependence on the environment) is equivalent to assume a screening mechanism so efficient (or so inefficient) that the transition of the scalaron field to its background value takes place at scales much larger (much smaller) than the cluster size.

3 The MAMPOSSt method

MAMPOSSt (Modelling Anisotropy and Mass Profiles of Observed Spherical Systems) is a method to derive mass profiles of galaxy clusters from the analysis of the dynamics of the

member galaxies under the assumption of spherical symmetry. In this section we describe the code, developed by ref. [23] and the modification we have made for the investigation of modified gravity models.

The *MAMPOSSt* method performs a Maximum-Likelihood fit to the distribution of the galaxies, assumed to be collisionless tracers of the gravitational potential, in the projected phase space (R, v_z), where R is the projected radius from the cluster center and v_z is the velocity along the line of sight (LOS), assuming a Gaussian 3D velocity distribution[1]. Given a parametric form of the mass profile $M(r)$, the velocity anisotropy profile $\beta(r) = 1 - \sigma_\theta^2/\sigma_r^2$ and the number density profile of the galaxies $\nu(r)$, the code solves the spherical Jeans' equation:

$$\frac{d\left[\nu(r)\sigma_r(r)\right]}{dr} + 2\beta(r)\frac{\nu(r)\sigma_r^2(r)}{r} = -\nu(r)\frac{d\Phi(r)}{dr}, \tag{3.1}$$

where $\Phi(r)$ is the time-time Bardeen potential, that coincides with the Newtonian potential in standard GR and $\sigma(r)$ is the velocity dispersion along the radial direction.

The solution of eq. (3.1) can be written as (e.g. ref. [38]):

$$\sigma(r) = \frac{1}{\nu(r)} \int_0^\infty \exp\left[2 \int_r^s \beta(t)\frac{dt}{t}\right] \nu(s)\frac{d\Phi(s)}{ds}ds. \tag{3.2}$$

Note that eq. (3.2) is the only relation in which the gravitational potential enters directly; we thus modified this expression by substituting $d\Phi/ds$ with the derivative of eq. (2.3). The solution is obtained in GR by assuming that the cluster is an isolated object. Ref. [39] showed that eq. (3.2) holds also in a cosmological ΛCDM background; since the additional contribution of fifth force tends to zero when the density reaches the background value and since we are looking for models that mimic the ΛCDM expansion history, we can safely assume that the solution of eq. (3.1) is still valid in modified gravity.

The probability density of observing an object at position (R, v_z) in the projected phase space is given by:

$$q(R, v_z) = \frac{2\pi R g(R, v_z)}{N_p(R_{max}) - N_p(R_{min})}, \tag{3.3}$$

with $N_p(R)$ the predicted number of galaxies with projected radius R and $g(R, v_z)$ is the surface density of observed objects with LOS velocity v_z that, in the case of a 3D-Gaussian velocity distribution, takes the form:

$$g(R, v_z) = \sqrt{\frac{2}{\pi}} \int_R^\infty \frac{r\nu(r)}{\sqrt{r^2 - R^2}} \frac{dr}{\sigma_r(r)\sqrt{1 - \beta(r)R^2/r^2}} \exp\left[-\frac{v_z^2}{2(1 - \beta(r)R^2/r^2)\sigma_r^2(r)}\right]. \tag{3.4}$$

The steps of the *MAMPOSSt* procedure could be summarized as follows:
(i) For a given choice of the parameter vector $\boldsymbol{\theta}$, the code computes $\sigma_r(r)$ over a logarithmic grid of points r_i and then performs a cubic-spline interpolation to evaluate for intermediate radii.
(ii) The solution of the Jeans equation is then used to get $g(R, v_z)$ for each $(R_i, v_{z,i})$. The integral of eq. (3.4) is numerically solved by assuming a cutoff for the upper limit of $\sim 15r_{200}$, where the velocity of the matter pushed by the Hubble flow is roughly 3σ above the mean value of the cluster. Variations of the viral radius by up to a factor of 2 do not change

---

[1] *MAMPOSSt* can be generally performed given any model of the 3D velocity distribution. The choice of a Gaussian is the most simple, but the code has been extensively tested to work quite well on halos drawn from cosmological simulations (see ref. [23])

significantly the result of the integration (ref. [23]).

(iii) The Likelihood is computed from eq. (3.3) by:

$$-\log \mathcal{L} = -\sum_{i=1}^{n} \log q(R_i, v_{z,i}|\boldsymbol{\theta}).$$ (3.5)

The minimum value of $-\log \mathcal{L}$ is found by searching over a grid in the parameter space. The implemented original version of *MAMPOSSt* can work with four free parameters, namley the scale radius of the tracers density profile r_ν, the parameter of the velocity anisotropy profile, the scale radius r_s and the radius r_{200} of the chosen parametric mass profile. We have expanded the parameter array in the case of modified gravity analysis by including 3 additional parameters, which are the interaction range $\lambda = 1/m$, h_1 and the screening radius S. In general we should consider also Q (see Sect. 2.1), but since we are looking at $f(R)$ models as a case study, in our modifed *MAMPOSSt* code Q is a constant fixed such that $2Q^2 = 1/3$. Furthermore, $h_1 = 1/(1+f_{,R})$; we restrict our analysis to the range $\lambda \leq 100$Mpc, which, for example, in the Hu & Sawicki model of $f(R)$ (ref. [3]) roughly corresponds to $|f_{,R}| < 10^{-3}$, so we can safely set $h_1 = 1$. We will upgrade the method for running with generic MG theories and other choices of the mass profile in future works.

We tested this modifed-*MAMPOSSt* code in the limit of standard gravity (i.e. $\lambda \to 0$) to reproduce the results of ref. [40] for MACS 1206; in the opposit situation ($\lambda \gg 1$) we checked that the modification in the mass profile reaches the maximum enhancement of $1/3$ as expected for $f(R)$ gravity (see Fig 1).

4   MACS 1206 and RXJ 2248

The galaxy clusters MACS 1206, at redshift $z = 0.44$, and RXJ 2248, at redshift $z = 0.35$, belong to a sample of 20 X-ray selected clusters for their apparent properties of dynamical relaxation, analyzed within the CLASH project (ref. [21]) and its spectroscopic follow-up CLASH-VLT (ref. [22]).

The analyses of ref. [41] and ref. [42] confirmed that MACS 1206 is a relaxed system with minor overdensities in the two-dimensional distribution and a negligible level of substructures within the cluster when the most conservative membership selection is used. Moreover, the mass profile derived by the *Chandra* X-ray data under the assumption of hydrostatic equilibrium of the intra-cluster medium is in agreement with the mass profile obtained by the Jeans' analysis of the dynamics of the galaxies inside the cluster (ref. [40]). Since the two determinations are both sensitive to the time-time Bardeen potential Φ, but the equilibrium is reached in different ways, the consistency between the two results is another indication of the relaxed state of the cluster.

The dynamical relaxation is further suggested by the concentric distribution of the stellar, gas and dark matter mass components, as argued in ref. [43].

The kinematic determination of the mass profile was carried on by ref. [40] which used spectroscopy information from the CLASH-VLT project (ref. [22]). From the sample of 2749 galaxies observed with VLT/VIMOS with reliable redshift measurements in the cluster field, 592 cluster members were identified after the rejection of interlopers.

Ref. [40] applied the *MAMPOSSt* method in the phase-space of the member galaxies to
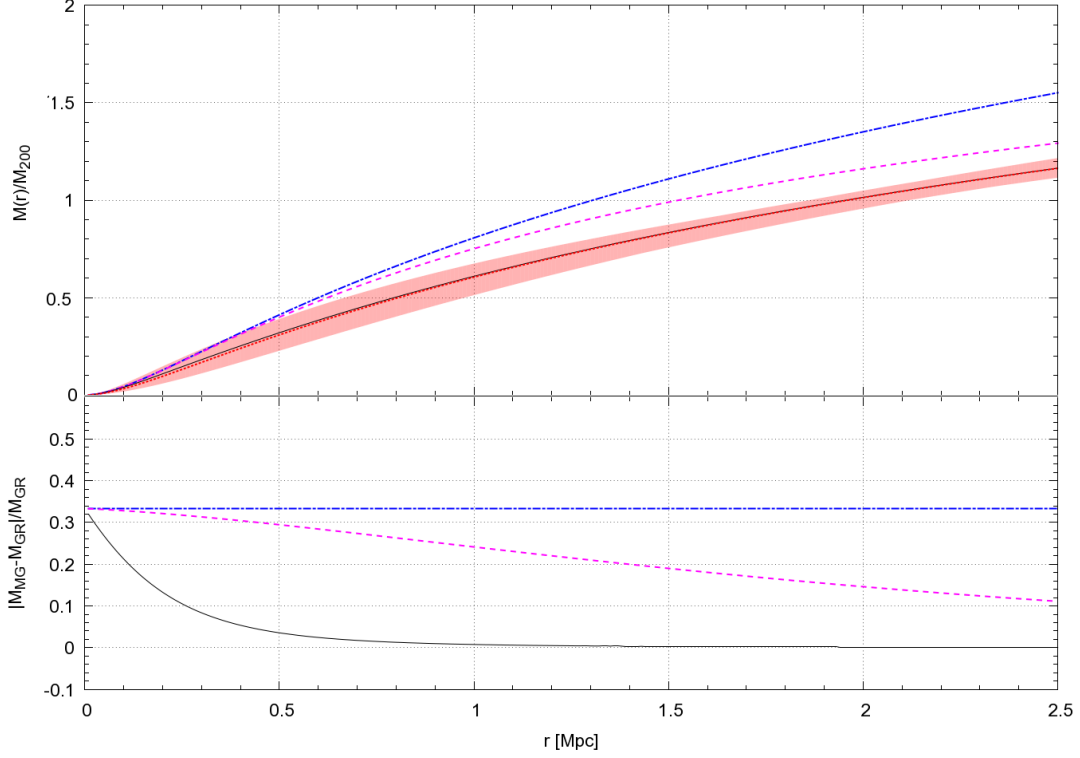
Figure 1. Upper panel: mass profiles in $f(R)$ gravity, expressed in unit of $M_{200} = 200H^2(z)r_{200}^3/2G$, for different values of the interaction range and $r_{200} = 1.96\,\mathrm{Mpc}$, $r_s = 0.27\,\mathrm{Mpc}$ (best fit values of the GR analysis of ref [40] for MACS 1206). Blue line-dotted curve: $\lambda = 1000\,\mathrm{Mpc}$,. Purple dashed curve: $\lambda = 1\,\mathrm{Mpc}$. Black solid curve: $\lambda = 0.1\,\mathrm{Mpc}$. The red shaded area shows the GR profile within the 68% C.L. in the NFW parameter with the best fit indicated by the red dashed curve. Lower panel: absolute enhancement with respect to the GR best fit profile. The lines correspond to the same values of λ as in the upper plot. For $\lambda \gg 1\,\mathrm{Mpc}$ the profile is enhanced by a factor $1/3$ with respect the GR value, while for $\lambda = 0.\,\mathrm{Mpc}1$ the result is very close to standard gravity.

estimate the mass profile up to the virial radius where the Jeans' equation is supposed to be valid. Three models for the anisotropy profile $\beta(r)$ have been taken into account, namely the Tiret model

$$\beta_T(r) = \beta_\infty \frac{r}{r + r_c}, \tag{4.1}$$

from ref. [44], the modified Tiret model

$$\beta_O(r) = \beta_\infty \frac{r - r_c}{r + r_c}, \tag{4.2}$$

and a model with constant anisotropy $\beta(r) = \beta_C$. In eqns. (4.1), (4.2) β_∞ represents the anisotropy value at large radii which is the free parameter entering in the *MAMPOSSt* analysis. r_c is assumed to coincide with the scale radius r_s of the anisotropy profile. This choice, as shown in ref. [45], provides a good fit to the average anisotropy profiles of galaxy clusters in a set of cosmological simulations.

Similary, ref. [40] considered different parametric expressions for the mass profile: the Einasto

model (ref. [46]), the NFW model, the Hernquist model (ref. [47]), the Burkert model (ref. [48]) and the softened isotermal sphere model (see e.g. ref. [49]). In the *MAMPOSSt* procedure the maximum value of the likelihood is obtained for the NFW profile; the combination of this mass model and the modified Tiret "O" anisotropy model gives the smallest product of the relative errors in r_s and r_{200} once marginalized over β.

Ref. [50] performed a first strong lensing analysis for MACS 1206 using 50 multiple images of 13 background sources, further upgraded by ref. [43], which combined strong lensing measurements with weak lensing shear and magnification information from *Subaru* multiband images out to $\sim 2\,\mathrm{Mpc}$. The resulting mass profile is parametrized as a NFW profile Additional lensing anlyses of the CLASH clusters involving also MACS 1206 were carried out by refs. [26, 51–53]; in this paper we refer to the results of ref. [26], that refined the joint shear-and-magnification weak-lensing analysis of ref. [52] by including *HST* strong-lensing information for a sample of 20 CLASH clusters.The weak+strong lensing results take into account model-dependent systematics of their strong-lensing modeling. Their error analysis also accounts for the intrinsic variations of the projected cluster lensing signal due to variations in cluster asphericity and the presence of correlated halos (see ref. [53]).

In the case of RXJ 2248 (first identified as Abell S1063 in ref. [54]), given its high mass and relatively high redshift, many lensing analyses have been performed: for the strong lensing analysis refs. [53, 55–58], and for the weak lensing analyses refs. [26, 52, 59–61]. The strong lensing mass profile used in this paper is an improvement of the one presented in [58]. They used a data set of 47 multiple images belonging to 16 families in a redshift range of $[0.1 - 6]$ detected down to $m_{F814W} = 26$. This data-set comes from the CLASH survey HST imaging, the CLASH-VLT spectroscopy with VIMOS-VLT, and obtained during the MUSE-VLT from MUSE science verification programme (ID 60.A-9345, P.I.:K. Caputi). As we did in the case of MACS1206, we use the weak lensing analysis of ref. [26] that combine weak lensing shear and magnification information from WFI 2.2m images out to $\sim 2.5\,\mathrm{Mpc}$. We combine the weak lensing information with the strong lensing ones from ref. [58]. The combined mass profile is parametrized with a NFW model.

As for the kinematic analysis we used the results obtained in Sartoris et al (in prep.) In this analysis they use a sample of 1233 galaxy members selected among more than 3700 galaxies with spectroscopic redshift provided by the VIMOS and MUSE observation out to $\sim 5\,\mathrm{Mpc}$. The MAMPOSSt technique has been applied using several anisotropy and mass profile models. Sartoris et al. in prep find that the best combination of models is the NFW mass profile with a Tiret velocity anisotropy model.

According to ref. [62], RXJ 2248 has undergone a recent off-axis merger. However, moderately deep X-ray Chandra (ref. [58]) observations do not show evidence of massive substructures in the inner region, but only a regular elongated shape, orientated like a large scale filament (ref. [61]).

5   Results

In this section we present our results for the constraints on the interaction range λ obtained from the analysis of the galaxy clusters MACS 1206 and RXJ 2248.

We apply the *MAMPOSSt* method to constrain $\lambda = 1/m_{eff}$ using the parametric expression of eq. (2.7) for the gravitational potential in generic $f(R)$ models (i.e. setting the

parameters as in eq. (2.25)) without screening, i.e. by assuming that the dependence of the enviroment of m_{eff} is negligible at the scales we are looking. In other words, we assume the screening radius to be much smaller - or much larger - than the cluster size. The situation could be also described in terms of a model with a strong screening mechanism where the effective mass of the scalaron remains always close to the minimum inside the overdensity.

For both clusters we include in the analysis data out to the virial radius, that is close to r_{200}, to ensure the validity of the Jeans equation. Moreover, the region below $r = 0.05\,Mpc$ is excluded since the internal dynamics of the Brightest Central Galaxy (BCG) becomes dominant (see e.g. ref. [63]).

5.1 MACS 1206

In the case of MACS 1206, for which 592 cluster members were identified in ref. [40], we use a sample of 345 galaxies, namely all the members lying within the radial range used in our analysis $[0.05\,\mathrm{Mpc} - 2.0\,\mathrm{Mpc}]$ in which we assume the Jeans' equation to be valid. The projected number density profile of the tracers $n(R)$ is fitted with a projected NFW (pNFW, ref. [64]) with a face value of the scale radius parameter $r_\nu = 0.63\,\mathrm{Mpc}^{+0.11}_{-0.09}$, as given by the Maximum Likelihood fit on the total sample of spectroscopic+photometric members (see Sect. 2.2 of ref. [40]).

We run the *MAMPOSSt* procedure in the modified gravity scenario with four free parameters, r_{200}, r_s, λ plus the velocity anisotropy parameter β. We use the "C" velocity anisotropy model (constant anisotropy with radius) as the reference model of our analysis, since it provides the highest probability in the *MAMPOSSt* fit in agreement with the GR results (see Table 2 of ref. [40])

In Figure 2 we show the marginalized likelihood distributions for the four free parameters in the case of $\beta(r) = const$. As in ref. [40], we consider the quantity $\sigma_r/\sigma_\theta = 1/\sqrt{1 - \beta}$ instead of β. The red curves are the results from the kinematic analysis while the blue curves represent the marginalized distributions when adding lensing information (see below). The vertical red solid lines indicate the best fit values given by *MAMPOSSt* for each parameter, compared with the GR best fit (black dashed lines). The red shaded regions in the r_s, r_{200} and β probability distributions show the 68% statistical errors. We obtain:

$$r_{200} = 1.98 \pm 0.11\,\mathrm{Mpc}, \qquad r_s = 0.39^{+0.40}_{-0.16}\,\mathrm{Mpc}, \qquad \beta \equiv \beta_C = 1.31^{+0.59}_{-0.19}, \qquad (5.1)$$

at 68% C.L., consistent with the results of [40]. This implies that the constraints on the standard parameters in GR are basically unffected by the introduction of the modified gravity term in the dynamical analysis with the *MAMPOSSt* method.

From the red curve in the bottom right panel of Fig. 2 it can be seen that the distribution of λ from the dynamics alone is almost flat; in the limit of $\lambda \to 0$ (i.e. $m_{eff} \to \infty$) this is not surprising, since we are approaching the GR regime and the contribution of M_{mg} in eq. (2.7) becomes negligible. To give an example, for $\lambda \leq 0.05\,\mathrm{Mpc}$ the increase in the mass profile at $r = 0.3\,\mathrm{Mpc}$ due to the fifth force is $\sim 10^{-4}$, that is undetectable if compared to the modification induced by the statistical uncertainties in r_s and r_{200}.

More interesting is the case $\lambda \gg 1\,\mathrm{Mpc}$, associated with considerable deviations from GR. The flattening behaviour of the curve for large λ is explained by looking at the degeneration directions in the two-dimensional distributions of Fig. 3. Each plot is obtained by marginalizing over the other two parameters; here the red and green lines indicate the
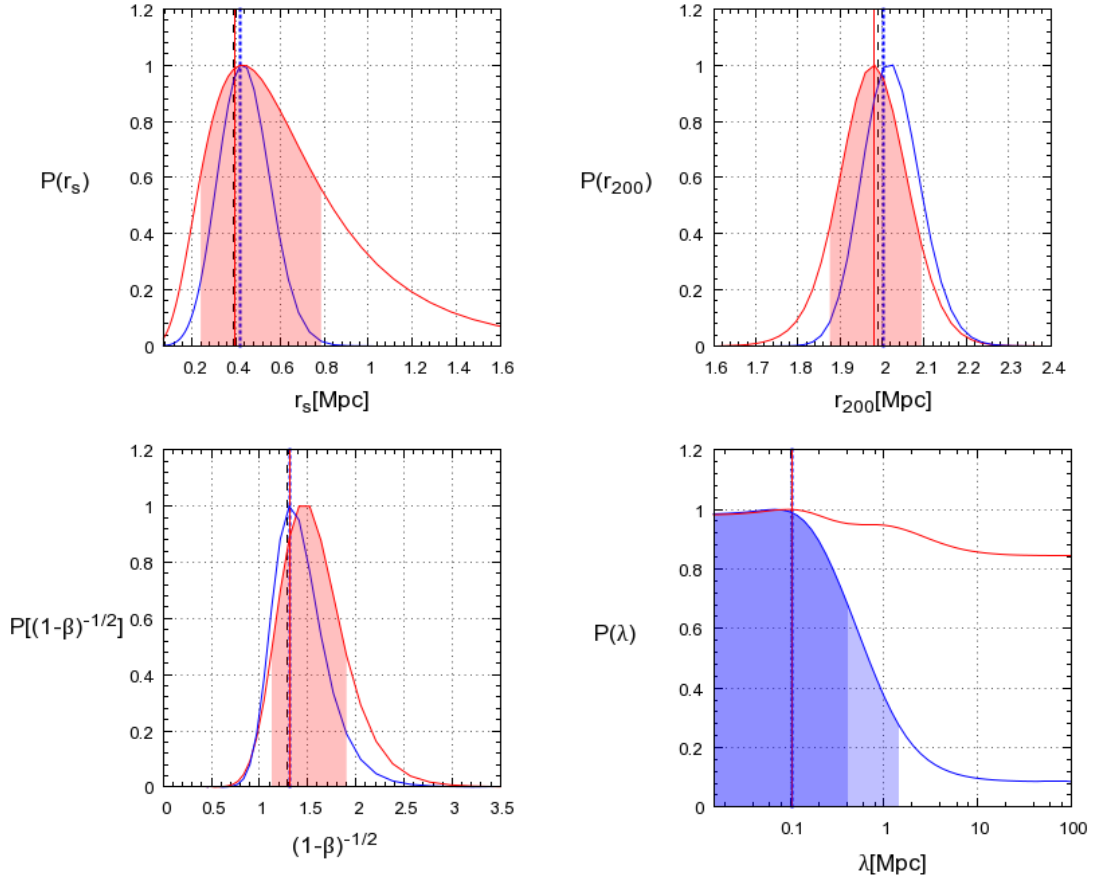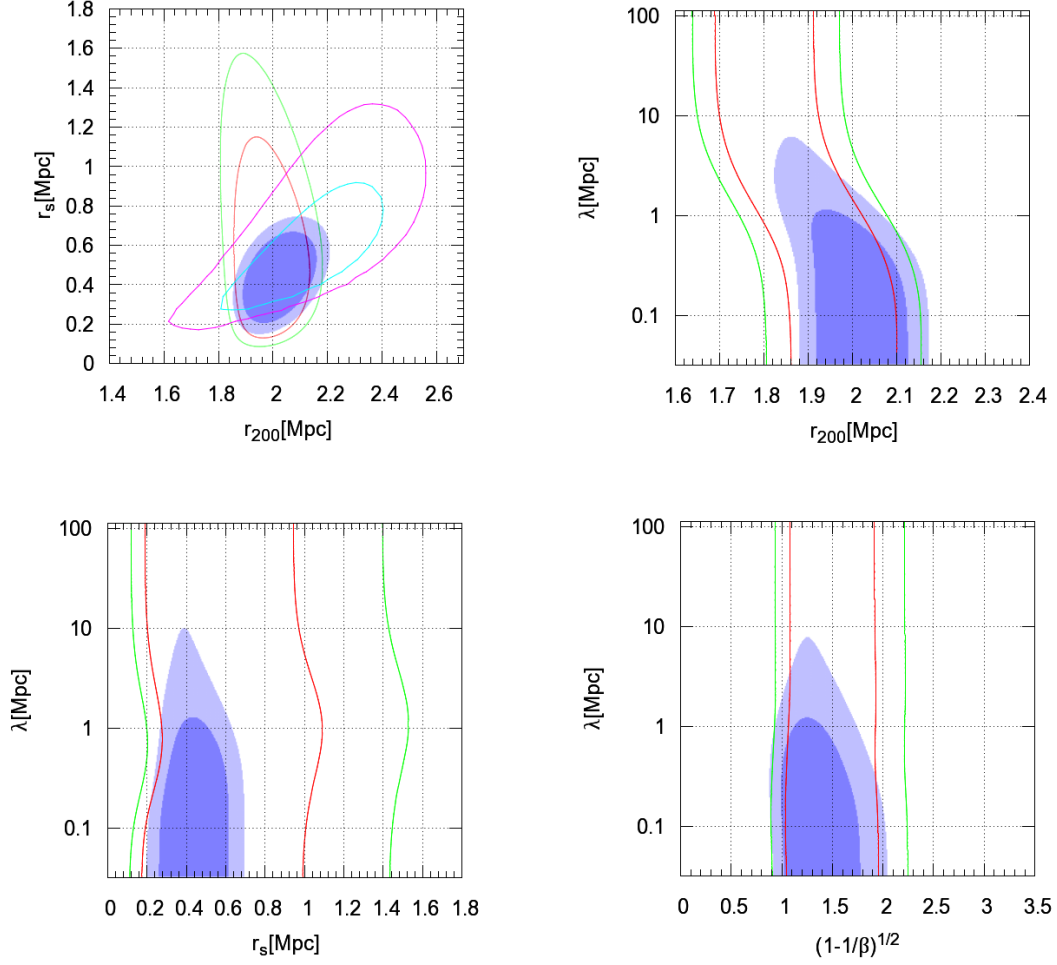
Figure 2. Likelihood distributions for the free parameters in the *MAMPOSSt* analysis obtained by marginalizing over the other three. Upper panels: r_s and r_{200}. Bottom panels: $\sigma_r/\sigma_\theta = 1/\sqrt{1-\beta}$ and $\lambda = 1/m_{eff}$. The red distributions are obtained from the kinematic analysis alone, while the blue curves show the joint lensing+kinematic results. Red and blue vertical lines represent the values corresponding to the maximum of the *MAMPOSSt* Likelihood and of $\mathcal{L}_{tot}$ respectively. Black solid lines are the best fit values of the GR analysis. Filled Red shaded areas in r_s, r_{200} and β indicate the 68% C.L. error from the dynamic analysis; the dark and light blue regions below the distribution of λ show the $\Delta\chi^2 = 1.0$ and the $\Delta\chi^2 = 2.1$ confidence intervals respectively.

dynamics contours at $\Delta\chi^2 = 2.3$, 4.61 (where $\chi^2 = -2\log[\mathcal{L}]$) respectively. As λ increases, the NFW paremeters tend to assume lower values; this is particulary evident for r_{200} while r_s shows only a slight change for $\lambda > 1$. This behaviour is a consequence of the relatively small maximum gain (up to $1/3$) produced in the mass profile by the additional force in $f(R)$ gravity. In fact, the effect generated by the term M_{mg} for large values of λ can be compensated by suitably adjusting r_s and r_{200} with respect to the GR values, so that the resulting modfied mass profile becomes very close to the GR one. Physically, this means that in $f(R)$ gravity the galaxy dynamics is altered in a similar way as the modification induced by a deeper potential well in GR, and even the high-quality data we are using are not sufficient to distinguish between the two cases.

The interaction range distribution shows a smooth peak at $\lambda = 0.1\,\mathrm{Mpc}$, corresponding to the best fit given by *MAMPOSSt*, but the excess of probability is statistically irrelevant.

Figure 3. Two-dimensional likelihood distributions obtained from the dynamical analysis alone (red and green contours) and from the total likelihood with lensing contribution (dark and ligth blue shaded areas) after marginalization over the other two parameters. Upper panels: r_{200} vs r_s, r_{200} vs λ. Bottom panels r_s vs λ, β vs λ. The inner contours/shaded regions correspond to the points within $\Delta\chi^2 \leq 2.3$ from the maximumx of the probability (roughly measuring the 68% C.L) while the outer contours/filled regions indicates points within $\Delta\chi^2 \leq 4.6$ (which represents the 90% C.L.). In the upper left panel the cyan and magenta lines show the $\Delta\chi^2 \leq 2.3$ and $\Delta\chi^2 \leq 4.61$ contours from the lensing analysis of ref. [26].

As discussed in Sect. 2.2, up to a conformal rescaling $(1 + f_{,R})^{-1}$, photons are affected only by the Newtonian contribution in $f(R)$ models. We thus can get additional information on the NFW parameters r_s and r_{200} by using the results of the gravitational lensing analysis presented in ref. [26].

In order to improve the derived constraints, we multiply the total likelihood distribution obtained by the *MAMPOSSt* method with the posterior probability distribution $P_{lens}(r_s, r_{200})$ given by strong+weak lensing analysis of [26] assuming flat prior in $\log(M_{200})$, $\log(c)$. Since

the lensing distribution peaks at $r_s = 0.53 \pm 0.18\,\mathrm{Mpc}$, $r_{200} = 2.14 \pm 0.16\,\mathrm{Mpc}$[2], favouring larger values of the NFW parameters compared to the *MAMPOSSt* result (see left panel of Fig. 3), the final likelihood, defined as

$$\log(\mathcal{L}_{tot}) = \log(\mathcal{L}_{dyn}) + \log(P_{lens}), \tag{5.2}$$

explores a region in the parameter space that is in the opposite direction with respect to the degeneracy direction in the dynamical analysis, thus increasing the significance of small deviations from GR. The new two-dimensional contours at $\Delta\chi^2 = 2.3$, 4.61, obtained by including the lensign prior, are shown by the dark and light blue regions in Fig. 3, while the marginalized distributions of $\mathcal{L}_{tot}$ are plotted as the solid blue curves in Fig. 2. The blue vertical dotted lines in each panel correspond to the maximum of the total likelihood $\mathcal{L}_{tot}$ including lensing informations. Now we can put an upper limit, after marginalization, on the effective scalaron interaction range $\lambda \leq 0.49\,\mathrm{Mpc}$ at $\Delta\chi^2 = 1.0$ (blue shaded area in the right bottom panel of Fig. 2) and $\lambda \leq 1.01\,Mpc$ at $\Delta\chi^2 = 2.71$ (light blue shaded area in the right bottom panel of Fig. 2), in agreement with the results of ref. [13] which indicate negligible deviations from GR for this cluster.

The analysis discussed above has been performed for our best fit model, NFW+"C", by assuming a fixed value for the scale radius of the number density profile of the tracers r_ν as the best fit value given by ref. [40]. We can asses now by how much the constraints are affected by a change of the anisotropy profile and of the parameter r_ν. To this purpose, we repeat the analysis for the other two anisotropy models mentioned, "T" and "O"; moreover, for our reference model we run *MAMPOSSt* with r_ν set to the extremes of the 68% confidence region obtained by the GR analysis of ref. [40]. The results are summarized in the first 5 rows of Table 5.2 while the marginalized distributions are shown in Fig. 4 and Fig. 5.

In each plot of both Figures the red lines are for the distributions obtained from the reference model "C" with $r_\nu = 0.63\,\mathrm{Mpc}$. In Fig. 4, the black dashed line shows the results for the "O" model, while the blue dotted curve is obtained from the "T" model. It is worth to notice that the best fit value of λ, as well as the position of the peak of the interaction range marginalized distribution, is not modified significantly by the different parametrization of the anisotropy profile. This is not surprising since λ is totally degenerate with β, as we can see from the right bottom plot of Fig. 3[3]. On the other hand, the shape of the distribution near the peak is affected by the changes in the anisotropy model. This is a consequence of the degeneration between λ and the scale radius r_s, which is responsible of the internal structure of the mass profile (right bottom panel of Fig. 3). In fact, the more the distribution in r_s is sharp, the more the peak in λ is evident.

Fig. 5 shows the effect of changing r_ν within the 68% C.L. given by the GR analysis. The relatively small statistical uncertainties with which r_ν is known produce a negligible effect on the marginalized distributions of the free parameters in our analysis. The black dashed curves in each plot indicate the results for r_ν set at the upper limit of the 68% confidence region, while the blue dotted curves are for r_ν set to the lower value. It's interesting that this last case ($r_\nu = 0.54\,\mathrm{Mpc}$) produce a likelihood slightly higher than the best fit $r_\nu = 0.63\,\mathrm{Mpc}$ (see Table 5.2), but we stress again that the scale radius is obtained by a fit which is external

---

[2]here the errors are estimated by approximating the distribution to a bivariate gaussian around the maximum of the probabilityNote that the maximum-likelihood values of r_{200} and r_s we find are slightly smaller than the values given in Table 2 of ref. [26]. This is because they quoted marginalized posterior constraints on the respective parameters obtained using the biweight location and scale estimators of ref. [65]

[3]We verified that this statement remains valid for the other two models analysed
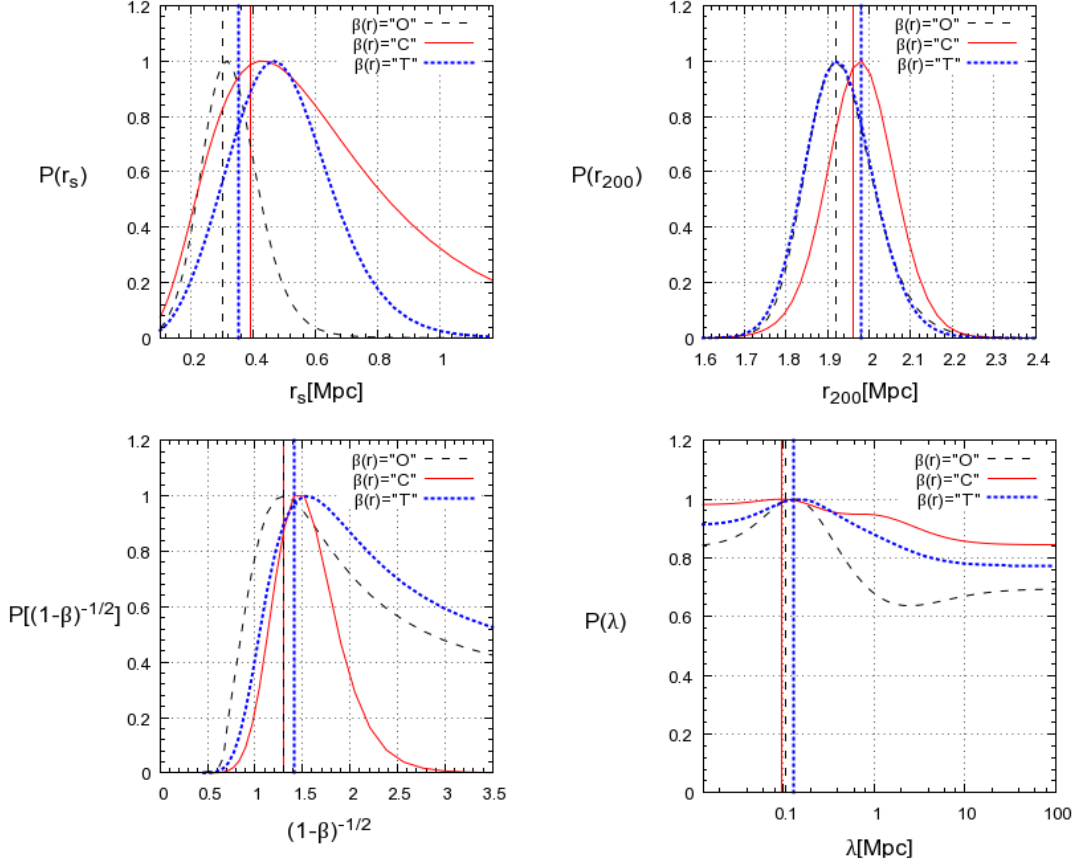
Figure 4. Marginalized likelihood distributions of r_{200}, r_s, $\sigma_r/\sigma_\theta = 1/\sqrt{1-\beta}$ and λ from the *MAMPOSSt* analysis obtained by changing the anisotropy model $\beta(r)$ for $r_\nu = 0.63$ Mpc. in the bottom left plot β indicates β_C for the "C" model and β_∞ for "T" and "O" models. Black dashed curves: "O" model. Red solid curves: "C" model. Blue dotted curves :"T" model. The corresponding vertical lines indicate the *MAMPOSSt* best fit of each free parameter.

to the *MAMPOSSt* procedure. The corresponding vertical lines indicate the values which maximize the likelihood $\mathcal{L}_{dyn}$.

To estimate the systematic uncertainties in our results on r_s, r_{200} and λ we take into account the variation caused by these changes. For the standard NFW parameters we obtain:

$$r_{200} = [1.98 \pm 0.11(stat) \pm 0.06(syst)]\,\mathrm{Mpc}, \qquad r_s = \left[0.39^{+0.40}_{-0.16}(stat) \pm 0.09(syst)\right]\,\mathrm{Mpc}, \tag{5.3}$$

where the statistical errors indicates the 68% confidence region as above, and the systematic errors are computed as the maximum difference between the best fit values (vertical lines). For $\beta \equiv \beta_C$ we can estimate only the variation induced by r_ν, since the parameter has a different meaning for each velocity anisotropy profile. As we can see from Fig. 5, no measurable effects are produced on the β distribution when r_ν is modified.

In the case of λ, we estimate the impact of systematics looking at the modifications in the upper bound after adding information from lensing analysis:

$$\lambda \le [1.61 + 0.30(syst)]\mathrm{Mpc} \qquad \Delta\chi^2 = 2.71, \tag{5.4}$$
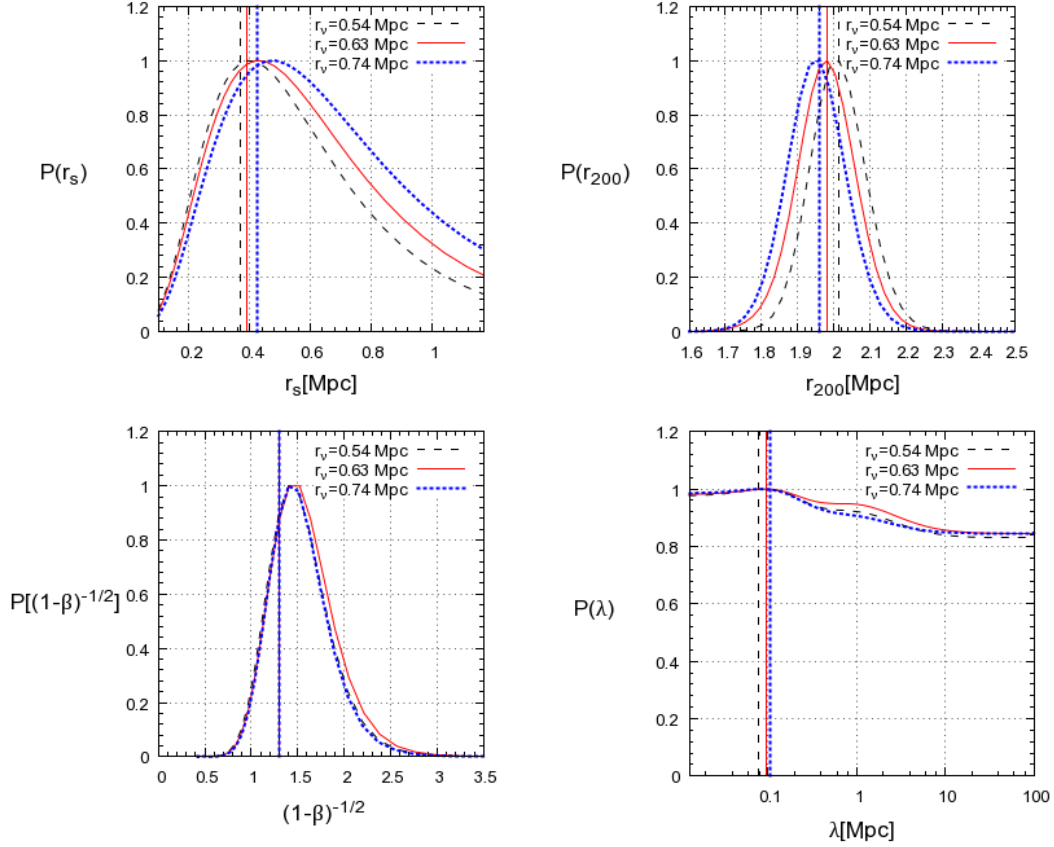
Figure 5. Marginalized likelihood distributions of r_{200}, r_s, $\sigma_r/\sigma_\theta = 1/\sqrt{1-\beta}$ and λ obtained for the reference model "C" by changing the scale radius of the number density profile of the galaxies r_ν within the 68% confidence region of the G.R. analysis. Red solid curves: r_ν fixed to the GR best fit value. Black dashed curves: r_ν fixed to the lower limit of the 68% confidence region. Blue dotted curves: r_ν (β_∞) settled to the upper limit of the 68% confidence region. The corresponding vertical lines indicate the *MAMPOSSt* best fit of each free parameter.

where the systematic uncertainty is the largest difference (in absolute value) between the upper limits obtained from the models analysed. The result is still compatible with small or negligible deviations from standard gravity.

5.2   RXJ 2248

We perform our analysis for the cluster RXJ 2248 in the radial range $[0.05\,\mathrm{Mpc} - 2.3\,\mathrm{Mpc}]$, using the 981 member galaxies lying in this region out of a sample of 1233 cluster members identified (Sartoris et al., in prep.).

As for MACS 1206, we fixed the number density profile whose parameter is given by the best fit value of the standard GR study (Sartoris et al., in prep.). In particular, the projected number density profile is again a pNFW with $r_\nu = 0.59 \pm 0.08\,\mathrm{Mpc}$, where this value is obtained by a Maximum Likelihood analysis on the spectroscopic members only. For $\beta(r)$ we use the same models discussed above; the highest probability for this cluster is given by the Tiret model "T" of eq. (4.1).
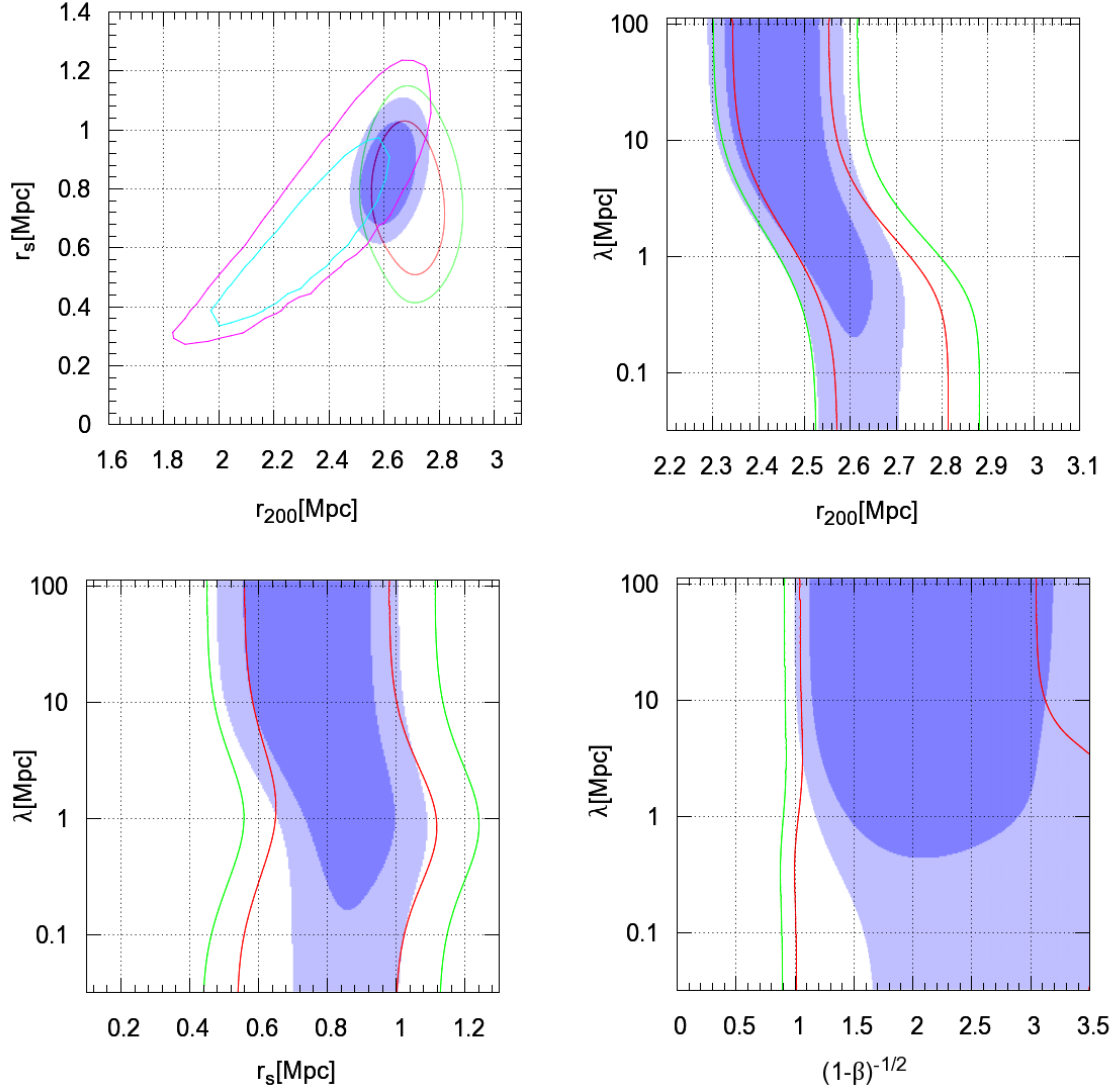
Figure 6. Results for RXJ 2248: two-dimensional contours at $\Delta\chi^2 \leq 2.3$ and $\Delta\chi^2 \leq 4.61$ from the maximum of the probability of the *MAMPOSSt* analysis (red and green lines respectively) and of the joint dynamics+lensing analysis (dark blue and light blue filled regions). The cyan and purple lines in the left upper panel show the lensing contours at 68% C.L. and 90% C.L.

The results of the *MAMPOSSt* procedure applied to the modified gravitational potential of eq. (2.7) with the velocity anisotropy model "T" are shown in Figs. 6 and 7. As before, the red and green curves in Fig. 6 indicate the contours at $\Delta\chi^2 = 2.3$ and $\Delta\chi^2 = 4.6$ respectively. The distributions for each parameter, obtained after marginalizing $\mathcal{L}_{dyn}$, are plotted as the red curves in Fig. 7.

The effective interaction range probability distribution (bottom right plot of Fig. 7) shows the same qualitative behaviour as found from the analysis of MACS 1206: the curve flattens both for large λ and for $\lambda \to 0$, altough the shape is more peaked near the *MAMPOSSt* best fit value $\lambda = 0.91$ Mpc (red vertical solid line) compared to the previous cluster. As mentioned above, the presence of the peak is strictly related to the distribution of the scale
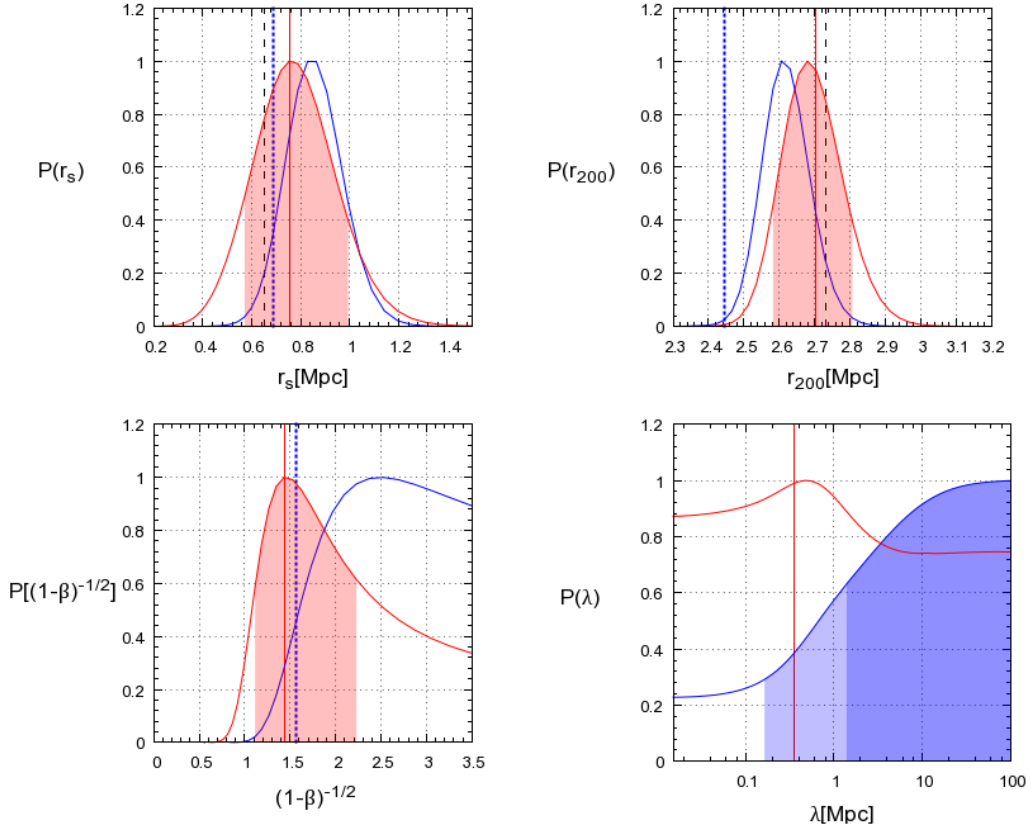
Figure 7. Results for RXJ 2248: single parameter distributions obtained by marginalizing the total likelihood over the other three. Upper panels: r_s and r_{200}. Bottom panels: $\sigma_r/\sigma_\theta = 1/\sqrt{1-\beta}$ and $\lambda = 1/m_{eff}$. Red curves: dynamics analysis, blue curves: lens+dyn. Vertical red solid lines indicate the *MAMPOSSt* best fit values, blue dotted lines correspond to the values maximizing the total likelihood while black dashed lines are the dynamics GR best fit. The filled areas below the marginalized distributions of r_s, r_{200} and $\beta = \beta_\infty$ represent the 68% C.L. of the dynamics results. The dark and light blue regions below the curve $P(\lambda)$ show the $\Delta\chi^2 \leq 1.0$ and $\Delta\chi^2 \leq 2.71$ confidence intervals, respectively.

radius r_s, which in this case is sharper than the one found from the analysis of the reference model for MACS 1206. Also the 2-dimensional degeneration directions with r_s, r_{200} and β (Fig. 6) are very similar to those of Fig. 3. The reason for a nearly constant, non-zero probability to have large deviations form GR can be again explained in terms of the small enhancement of the mass profile produced by the fifth force, which allows λ to be large if r_s and r_{200} change in such a way to compensate the effect of the additional term. It is worth to point out that the number of galaxies used in the *MAMPOSSt* fit for this cluster is about three times larger than that of MACS 1206; this means that roughly tripling the statistics is still not sufficient to set meaningful constraints on λ from the analysis of dynamics alone.

As for the standard NFW parameters and the velocity anisotropy, we obtain the results:

$$r_{200} = 2.70^{+0.10}_{-0.14}\,\mathrm{Mpc}, \qquad r_s = 0.75^{+0.14}_{-0.18}\,\mathrm{Mpc}, \qquad \beta_\infty = 1.43^{+0.59}_{-0.19}, \tag{5.5}$$

at 68% C.L., where the errors are computed with respect to the best fit values of the *MAM-*

POSSt procedure (red vertical solid lines in Fig. 7). The constraints are consistent with the results obtained from the GR analysis (Sartoris et al., in prep.) $r_{200} = 2.73^{+0.08}_{-0.09}$ Mpc, $r_s = 0.65^{+0.12}_{-0.22}$ Mpc and $\beta_\infty = 1.43^{+1.07}_{-0.24}$ (black dashed lines in Fig. 7). Nevertheless, there is a modest difference between the GR and MG best fit values, suggesting that the impact of the interaction range λ on the total likelihood distribution is larger than for MACS 1206. Since the best fit is sensitive to every small variation in the probability, the slight preference of $\lambda \sim 0.3$ (roughly three times the value from the best fit obtained in the previous case) is sufficient to move away the other parameters from the GR values, but the excess is still not relevant enough to affect the marginalized distributions which remain in agreement with the analysis of Sartoris et al. (in prep.).

Following the same approach as in Sect. 5.1, we combine the likelihood distribution generated by the *MAMPOSSt* method with the lensing posterior probability distribution $P(r_{200}, r_s)$ derived from the results of [26] and Caminha et al. (in prep). The blue contours and the blue lines of Figure 7 show what we obtain from the analysis of $\mathcal{L}_{tot}$ defined in eq. (5.2). No upper limits can be provided for λ in this case. On the contrary, the joint kinematic+lensing study indicates a preference for large values of the effective interaction range, excluding at $\Delta\chi^2 = 2.71$ the region $\lambda \leq 0.14$ Mpc, as we can see from the marginalized distribution in the right bottom panel.

The origin of this behaviour is related to a slight tension between the lensing and dynamics probability distributions in the plane (r_s, r_{200}). Indeed, $P_{lens}(r_{200}, r_s)$ exhibits a peak for $r_{200} = 2.24 \pm 0.22$ Mpc, $r_s = 0.55 \pm 0.27$ Mpc (see the purple contours in the upper left panel of Fig. 7), while the 2-dimensional dynamics distribution has a maximum for $r_s = 0.64$ Mpc and $r_{200} = 2.65$ Mpc. When combining the 2 analyses, we increase the probability in the region of parameter space corresponding to relatively large λ values, while decreasing the probability for a vanishing interaction range, as can be seen from the 2 dimensional distributions of Fig. 6.

As before, we now study the effect of changing the scale radius of the tracers r_ν within the 68% C.L. of the GR analysis and the anisotropy model $\beta(r)$. Fig. 8 shows the effect on the marginalized distributions due to the different parametrization of the anisotropy profile while Fig. 9 displays the changes induced by r_ν. The red curves in both Figures indicate the reference model ("T" in this case) with $r_\nu = 0.59$ Mpc. Again, the largest effect on the results is obtained when changing the anisotropy model (Fig. 8). In this case both the position and the shape of the peak in the distribution of λ are modified as a consequence of the variations in the r_s marginalized likelihood; this is particularly evident for the model "O" which shows the largest discrepancy in the best fit value of r_s compared to the reference model (vertical lines in the upper left plot of Fig. 8, see also Table 5.2). Nevertheless, the tension with lensing results is not resolved when including these systematics. As shown in the five bottom rows of Table 5.2, all the runs provide a lower limit on λ which is larger than the reference model, except for the case of $r_\nu = 0.66$ Mpc where the constraint on the interaction range relaxes from $\lambda \geq 0.30$ to $\lambda \geq 0.06$ Mpc at $\Delta\chi^2 = 2.71$.

Note that the results for $r_\nu = 0.54$ Mpc is slightly preferred with respect to the case of $r_\nu = 0.59$ Mpc (last row in Table 5.2), similarly of what we found for MACS 1206. In order to take into account the variation induced on the NFW parameters r_s, r_{200} by the changes in the anisotropy profile and in the scale radius of the number density profile, we consider the maximum difference between the best fit values of each run and of the reference model:

$$r_{200} = [2.70^{+0.10}_{-0.14}(stat) \pm 0.04(syst)]\, \text{Mpc}, \qquad r_s = [0.75^{+0.14}_{-0.18} \pm 0.20(syst)]\, \text{Mpc}. \qquad (5.6)$$
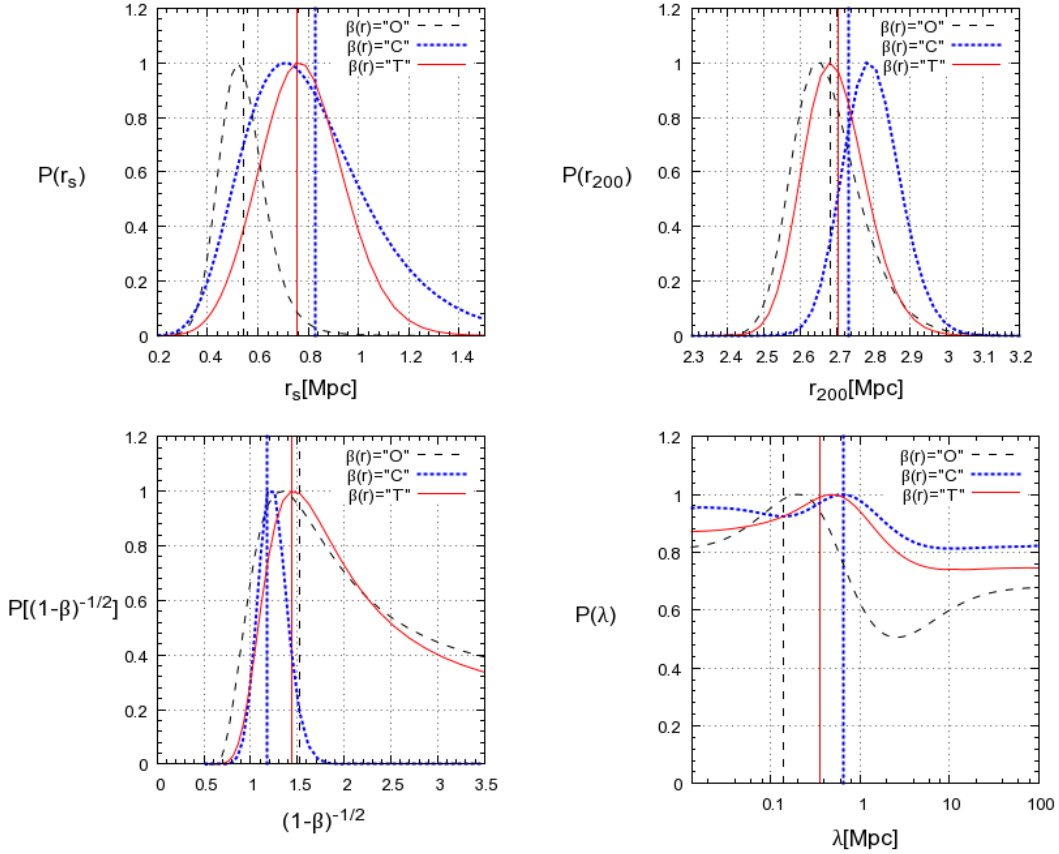
Figure 8. Effects on the marginalized likelihood distributions of r_{200}, r_s, $\sigma_r/\sigma_\theta = 1/\sqrt{1-\beta}$ and λ from the dynamics analysis of RXJ 2248 when changing the anisotropy model $\beta(r)$. Red solid curves: reference model "T". Black dashed curves: "O" model. Blue dotted curves: "C" model. The corresponding vertical lines indicate the *MAMPOSSt* best fit of each free parameter. In the bottom left plot, $\beta \equiv \beta_\infty$ for the "T" and the "O" models, while $\beta \equiv \beta_C$ for the "C" model.

As we did for the previous cluster, we estimate the systematic uncertainties in β_∞ from the variation induced by r_ν only, obtaining:

$$\beta_\infty = 1.43^{+0.59}_{-0.19}(stat) \pm 0.10(syst). \tag{5.7}$$

6 Discussion and conclusions

In this work we have developed a procedure to constrain modifications of gravity at the scales of galaxy clusters by determining the time-time gravitational potential $\Phi(r)$ from the analysis of the dynamics of the galaxies in the cluster. We have focused on a particular sub-class of scalar-tensor theories, the $f(R)$ models, where the additional degree of freedom associated to the modification of gravity is expressed in terms of the interaction range λ; we have applied our method to the case of two dynamically relaxed clusters MACS 1206 at $z = 0.44$ and RXJ 2248 at $z = 0.35$, extensively analysed within the CLASH/CLASH-VLT collaborations. Assuming spherical symmetry, we have parametrized the cluster mass density profile as a
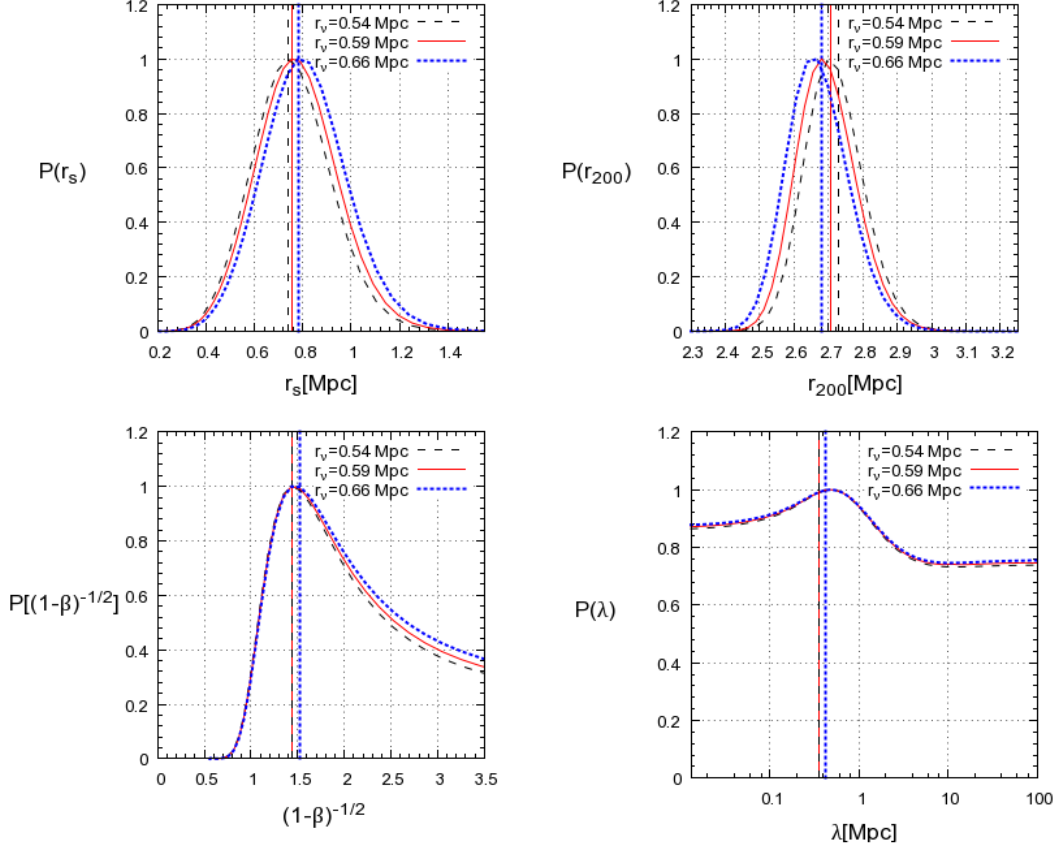
Figure 9. Effects on the marginalized likelihood distributions of r_{200}, r_s, $\sigma_r/\sigma_\theta = 1/\sqrt{1-\beta}$ and λ of the dynamics analysis of RXJ 2248 for the reference model "T" when changing the scale radius of the number density profile of the galaxies r_ν within the 68% confidence region of the GR analysis. Red solid curves: r_ν fixed to the GR best fit value. Black dashed curves: r_ν fixed to the lower limit of the 68% confidence region. Blue dotted curves: r_ν settled to the upper limit of the 68% confidence region. The corresponding vertical lines indicate the *MAMPOSSt* best fit of each free parameter.

NFW profile, charcterized by the scale radius r_s and the virial radius r_{200}, constraining the vector of parameters (r_s, r_{200}, λ) with the modified *MAMPOSSt* code explained in Sect. 3. Since in $f(R)$ gravity photons are not affected by the fifth force contribution we have further combined our results with the information on the NFW parameters r_s, r_{200} from the strong+weak lensing analysis of ref. [26].

The results for the cluster MACS 1206 are in agreement with the GR predictions, confirming the previous analysis of ref. [13]. When including lensing contribution, we obtain an upper limit of $[\lambda \leq 1.61(stat) + 0.30(syst)\,\mathrm{Mpc}$ at $\Delta\chi^2 = 2.71$; the bound takes into account variations in the velocity anisotropy profile $\beta(r)$ and in the scale radius of the galaxy number density profile r_ν, which enters in the kinematic determination of the gravitational potential (or, equivalently, of the mass profile).

A peculiar behaviour has instead been found in the case of RXJ 2248, where the joint kinematic+lensing analysis shows a 2σ preference for values of λ larger than 0. Including also sytematic effects due to changes in the anisotropy profile $\beta(r)$ and in r_ν, we get a lower bound $\lambda \geq 0.12\,\mathrm{Mpc}$ at $\Delta\chi^2 = 2.71$. This result arises from a mild tension $< 1\sigma$ between the

Anis. model	r_ν [Mpc]	r_{200} [Mpc]	r_s [Mpc]	$(1 - \beta_{C/\infty})^{-1/2}$	λ [Mpc]	$\Delta\chi^2$
		MACS 1206				
C	**0.63**	1.98 ± 0.11	$0.39^{+0.40}_{-0.16}$	$1.31^{+0.59}_{-0.19}$	≤ 1.61	0.0
O	0.63	$1.93^{+0.09}_{-0.12}$	$0.30^{+0.14}_{-0.07}$	$1.51^{+0.69}_{-0.55}$	≤ 1.31	0.72
T	0.63	$1.96^{+0.07}_{-0.14}$	$0.35^{+0.33}_{-0.04}$	$1.41^{+1.35}_{-0.29}$	≤ 1.31	0.20
C	0.74	$1.96^{+0.11}_{-0.10}$	$0.42^{+0.42}_{-0.18}$	$1.31^{+0.59}_{-0.18}$	≤ 1.31	0.20
C	0.54	$2.01^{+0.14}_{-0.07}$	$0.42^{+0.28}_{-0.12}$	$1.31^{+0.59}_{-0.19}$	≤ 1.78	-0.14
		RXJ 2248				
T	**0.59**	$2.70^{+0.10}_{-0.14}$	$0.75^{+0.14}_{-0.18}$	$1.43^{+0.79}_{-0.24}$	≥ 0.14	0.0
O	0.59	$2.68^{+0.10}_{-0.14}$	$0.55^{+0.11}_{-0.14}$	$1.53^{+0.71}_{-0.55}$	≥ 0.84	0.64
C	0.59	$2.74^{+0.15}_{-0.06}$	$0.83^{+0.21}_{-0.32}$	$1.18^{+0.25}_{-0.14}$	≥ 0.80	0.44
T	0.66	2.67 ± 0.12	$0.78^{+0.26}_{-0.19}$	$1.53^{+0.69}_{-0.34}$	≥ 0.06	0.20
T	0.54	$2.73^{+0.09}_{-0.15}$	$0.74^{+0.24}_{-0.19}$	$1.43^{+0.66}_{-0.24}$	≥ 0.19	-0.16

Table 1. Results on the free parameters of our analysis for the cluster MACS 1206 (first 5 rows) and RXJ 2248 (last 5 rows). The bold characters indicate the reference models adopted for each of the two clusters. The errors in r_{200}, r_s and $\sigma_r/\sigma_\theta = 1/\sqrt{1-\beta}$ are the 68% C.L. from the *MAMPOSSt* procedure; the upper(lower) limits on λ are obtained at $\Delta\chi^2 = 2.71$ from the joint kinematic+lensing analysis. The last coloumn indicate the logarithmic difference between the likelihood of the model analysed and the likelihood of the reference model.

dynamics and lensing determinations of the mass profile in GR. Larger values of r_s and r_{200} are favoured by the dynamics analysis with respect to the lensing results; the discrepancy could be interpreted as the additional contribution of the fifth force which affects only the motion of non-relativistic particles. In order to better investigate the effect of this tension on the Bardeen potential Φ and Ψ, we compute the anisotropic stress $\eta = \Psi/\Phi$ in the radial range covered by our analysis, following the approach of ref. [13]. The results are shown in Fig. 10, where the blue and light blue areas represent the 68% and the 90% confidence regions, respectivelty. As we can see, the discrepancy with the GR expected value $\eta = 1$ is at more than 1σ for $r \gtrsim 1\,\mathrm{Mpc}$. For $r = 2.3\,\mathrm{Mpc}$ we obtain $\eta = 0.57 \pm 0.42$ at 90% C.L. Interestingly, this is in agreement with the prediction of $f(R)$ models, in which the anisotropic stress is smaller than 1, reaching the value $\eta = 1/2$ in the case of maximum deviations from GR.

The results from the analysis of RXJ 2248 point in the opposite direction of what we
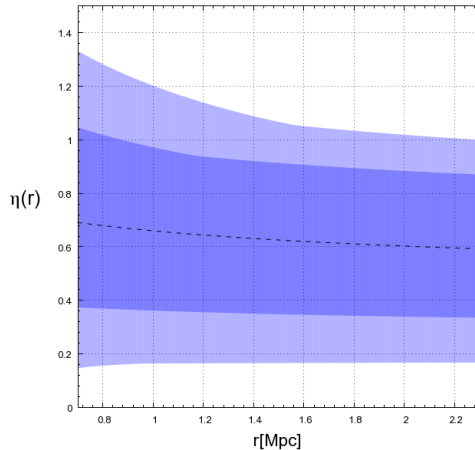
Figure 10. Anisotropic stress η in the radial range $[0.7\,\mathrm{Mpc} - 2.3\,\mathrm{Mpc}]$ for the cluster RXJ 2248. The blue shaded region indicates the 68% C.L. while the light blue area is the 90% C.L. The best fit profile is given by the black dashed line.

have obtained for MACS 1206 (altough the constraints we have derived on λ from the 2 clusters are still compatible within the 90% C.L.), highlighting the need to check the systematics associated to the assumptions on which our method relies. The presence of possible substructures and departures from spherical symmetry could in principle affect both the dynamics and lensing analyses; nonetheless, we stress again that both clusters belong to a sample of 20 X-rays selected objects for their properties of apparent dynamical relaxation.

It is important to point out that we have considered only $f(R)$ models in which the screening mechanism works at scales smaller (or much larger) than those investigated here, so that we could neglect the dependence of $m_{f_R} = 1/\lambda$ on the local density.

In order to translate our results in a bound on the background scalaron field $|\bar{f}_{,R}|$, we have to take into account how the chameleon screening works once a particular model is fixed. As an example, we focus on the Hu & Sawicki model of ref. [3], in which the functional form of $f(R)$ can be approximated by a power law:

$$f(R) \simeq 6\Omega_\Lambda - \frac{f_{,R0}}{n}\frac{R_{0,b}^{n+1}}{R^n}, \tag{6.1}$$

where we set $n = 1$; $f_{,R0} < 0$ is the background scalaron value at present day. An accurate treatment of this situation requires a full numerical solution of the nonlinear equation (2.17); we follow here a simple analytical approximation to describe the screening mechanism in this case, just to show what we can obtain with our method. We model the chameleon regime with an instantaneous transition between the region of full screening $r \leq S$, where $f_{,R} = 0$, and the linear region $r > S$, where the Newtonian potential is modified according to eq. (2.24). As explained in ref. [66], this can be achieved by taking $\delta f_{,R} = \min(\delta f_{,R}^{lin}, |\bar{f}_{,R}|)$, where $\delta f_{,R}^{lin}$ is the solution of the field equation with the linearization condition (2.23). Running again the *MAMPOSSt* procedure and combining the resulting likelihood with the lensing posterior we get $\bar{\lambda}_{f_R} \leq 20\,\mathrm{Mpc}$ and $\bar{\lambda}_{f_R} \geq 12\,\mathrm{Mpc}$ at $\Delta\chi^2 = 2.71$ for MACS 1206 and RXJ 2248, respectively. Now $\bar{\lambda}_{f_R}$ is related to the background field value through eq. (2.19), which is
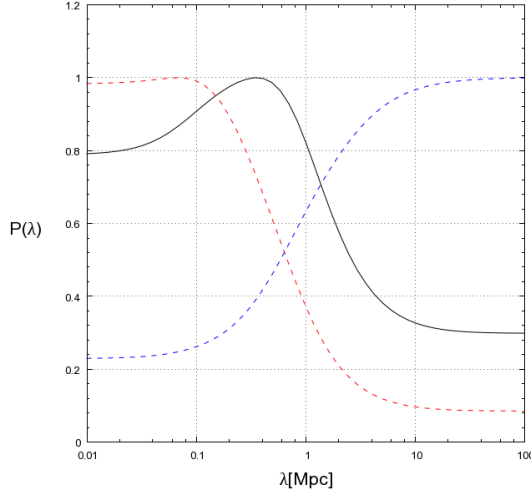
Figure 11. Black solid line: combined likelihood obtained by multipliyng the marginalized probability distributions from the analysis of the reference model for MACS1206 (red dashed line) and for RXJ 2248 (blue dashed line).

so constrained to be $|\bar{f}_{,R}(z = 0.44)| \leq 4.0 \times 10^{-5}$ and $|\bar{f}_{,R}(z = 0.35)| \geq 1.4 \times 10^{-5}$. The first bound is in agreement with current determinations of the magnitude of the background scalaron, obtained using distance indicators at low-redshift (ref. [67]), galaxy cluster abundance (refs. [14, 68]) and redshift space distortions (ref. [69]), which have tightened the upper limit up to $|\bar{f}_{,R0}| < 10^{-6}$, compatible with very small deviations from GR. On the other hand, is not surprising that the effect of introducing screening for RXJ 2248 is to increase the tension we found, leading to a value of $|\bar{f}_{,R0}|$ for this particular model which is totally inconsistent with other constraints.

As the results we obtained are not in contradiction, we can in principle assume that the interaction range is constant in time between the redshifts of MACS 1206 and RXJ 2248 and combine the marginalized likelihood of λ derived from the analysis of the reference model for each cluster. As we can see in Fig. 11, the apparent tension with GR is relaxed and we can still put an upper limit of $\lambda \leq 1.81$ Mpc at $\Delta\chi^2 = 1.0$. In conclusion is clear that although two clusters are obviously too few to produce stringent constraints, they are already sufficient to show the potential of the method of combining dynamics and lensing to test gravity. On the other hand, the tension we have highlighted shows that it is necessary to model accurately the velocity anisotropy and to take into account deviations from spherical symmetry and from virialization before the method can be claimed to give a robust determination of the anisotropic stress η and its scale dependence. This can be achieved by the analysis of simulated clusters, both in GR and in modified gravity, to better understand how the above mentioned effects influence our constraints. As a first step in this direction, in a subsequent work we will estimate how many cluster similar to the one employed here are necessary in order to constrain at the same time the profile parameters, the velocity anisotropy, and the modified gravity parameters.

Moreover, it is worth to notice that the analysis presented in this paper can be extended to all the generic scalar-tensor theories where the coupling constant Q is not fixed and the

lensing potential is still given by the Newtonian potential $(\Phi + \Psi)/2 = \Phi_N$ (e.g. the Brans-Dicke k-essence (BDK) model of ref. [70]), but the data we used here are not sufficient to get significant information on this kind of models.

Future imaging surveys, both from ground (e.g. LSST) and from space-borne telescopes (e.g. Euclid and WFIRST) will provide lensing mass reconstructions for thousands of clusters, although at a signal-to-noise level lower than that reached by the two clusters considered here. At the same time, the next generation of high-multiplexing spectrographs on 8m-class telescopes will allow a precise characterisation of the phase-space structure for a sizeable fraction of such clusters. This increase in statistics calls for the need of controlling the above mentioned systematics in the recovery of mass profiles from lensing and internal cluster dynamics, if we want to take full advantage of the their potentiality as powerful diagnostics for the nature of gravity on cosmological scales.

References

[1] A. G. Riess, A. V. Filippenko, P. Challis, A. Clocchiatti, A. Diercks, P. M. Garnavich, R. L. Gilliland, C. J. Hogan, S. Jha, R. P. Kirshner, B. Leibundgut, M. M. Phillips, D. Reiss, B. P. Schmidt, R. A. Schommer, R. C. Smith, J. Spyromilio, C. Stubbs, N. B. Suntzeff, and J. Tonry, *Observational Evidence from Supernovae for an Accelerating Universe and a Cosmological Constant*, AJ **116** (Sept., 1998) 1009–1038, [`astro-ph/9805201`].

[2] S. Perlmutter, G. Aldering, G. Goldhaber, R. A. Knop, P. Nugent, P. G. Castro, S. Deustua, S. Fabbro, A. Goobar, D. E. Groom, I. M. Hook, A. G. Kim, M. Y. Kim, J. C. Lee, N. J. Nunes, R. Pain, C. R. Pennypacker, R. Quimby, C. Lidman, R. S. Ellis, M. Irwin, R. G. McMahon, P. Ruiz-Lapuente, N. Walton, B. Schaefer, B. J. Boyle, A. V. Filippenko, T. Matheson, A. S. Fruchter, N. Panagia, H. J. M. Newberg, W. J. Couch, and T. S. C. Project, *Measurements of Ω and Λ from 42 High-Redshift Supernovae*, ApJ **517** (June, 1999) 565–586, [`astro-ph/9812133`].

[3] W. Hu and I. Sawicki, *Models of f(R) cosmic acceleration that evade solar system tests*, Phys. Rev. D **76** (Sept., 2007) 064004, [`arXiv:0705.1158`].

[4] G. Dvali, S. Hofmann, and J. Khoury, *Degravitation of the cosmological constant and graviton width*, Phys. Rev. D **76** (Oct., 2007) 084006, [`hep-th/0703027`].

[5] A. Lue, R. Scoccimarro, and G. Starkman, *Differentiating between modified gravity and dark energy*, Phys. Rev. D **69** (Feb., 2004) 044005, [`astro-ph/0307034`].

[6] G.-B. Zhao, L. Pogosian, A. Silvestri, and J. Zylberberg, *Searching for modified growth patterns with tomographic surveys*, Phys. Rev. D **79** (Apr., 2009) 083513, [`arXiv:0809.3791`].

[7] B. Hu, M. Liguori, N. Bartolo, and S. Matarrese, *Parametrized modified gravity constraints after Planck*, Phys. Rev. D **88** (Dec., 2013) 123514, [`arXiv:1307.5276`].

[8] G.-B. Zhao, T. Giannantonio, L. Pogosian, A. Silvestri, D. J. Bacon, K. Koyama, R. C. Nichol, and Y.-S. Song, *Probing modifications of general relativity using current cosmological observations*, Phys. Rev. D **81** (May, 2010) 103510, [`arXiv:1003.0001`].

[9] Planck Collaboration, P. A. R. Ade, N. Aghanim, M. Arnaud, M. Ashdown, J. Aumont, C. Baccigalupi, A. J. Banday, R. B. Barreiro, N. Bartolo, and et al., *Planck 2015 results. XIV. Dark energy and modified gravity*, ArXiv e-prints (Feb., 2015) [arXiv:1502.01590].

[10] K. Yamamoto, B. A. Bassett, R. C. Nichol, Y. Suto, and K. Yahata, *Searching for modified gravity with baryon oscillations: From SDSS to wide field multiobject spectroscopy (WFMOS)*, Phys. Rev. D **74** (Sept., 2006) 063525, [astro-ph/0605278].

[11] E. Jennings, C. M. Baugh, B. Li, G.-B. Zhao, and K. Koyama, *Redshift-space distortions in f(R) gravity*, MNRAS **425** (Sept., 2012) 2128–2143, [arXiv:1205.2698].

[12] S. Ferraro, F. Schmidt, and W. Hu, *Cluster abundance in f(R) gravity models*, Phys. Rev. D **83** (Mar., 2011) 063503, [arXiv:1011.0992].

[13] L. Pizzuti, B. Sartoris, S. Borgani, L. Amendola, K. Umetsu, A. Biviano, M. Girardi, P. Rosati, I. Balestra, G. B. Caminha, B. Frye, A. Koekemoer, C. Grillo, M. Lombardi, A. Mercurio, and M. Nonino, *CLASH-VLT: testing the nature of gravity with galaxy cluster mass profiles*, J. Cosmology Astropart. Phys. **4** (Apr., 2016) 023, [arXiv:1602.03385].

[14] M. Cataneo, D. Rapetti, F. Schmidt, A. B. Mantz, S. W. Allen, D. E. Applegate, P. L. Kelly, A. von der Linden, and R. G. Morris, *New constraints on f (R) gravity from clusters of galaxies*, Phys. Rev. D **92** (Aug., 2015) 044009, [arXiv:1412.0133].

[15] E. Di Valentino, A. Melchiorri, and J. Silk, *Cosmological hints of modified gravity?*, Phys. Rev. D **93** (Jan., 2016) 023513, [arXiv:1509.07501].

[16] C. M. Will, *The Confrontation between General Relativity and Experiment*, Living Reviews in Relativity **9** (Mar., 2006) [gr-qc/0510072].

[17] J. Khoury, *Theories of Dark Energy with Screening Mechanisms*, ArXiv e-prints (Nov., 2010) [arXiv:1011.5909].

[18] L. Amendola, *Coupled quintessence*, *Phys. Rev. D* **62** (Jul, 2000) 043511.

[19] G. W. Horndeski, *Second-order scalar-tensor field equations in a four-dimensional space*, *International Journal of Theoretical Physics* **10** (1974), no. 6 363–384.

[20] J. Khoury and A. Weltman, *Chameleon cosmology*, Phys. Rev. D **69** (Feb., 2004) 044026, [astro-ph/0309411].

[21] M. Postman, D. Coe, N. Benítez, L. Bradley, T. Broadhurst, M. Donahue, H. Ford, O. Graur, G. Graves, S. Jouvel, A. Koekemoer, D. Lemze, E. Medezinski, A. Molino, L. Moustakas, S. Ogaz, A. Riess, S. Rodney, P. Rosati, K. Umetsu, W. Zheng, A. Zitrin, M. Bartelmann, R. Bouwens, N. Czakon, S. Golwala, O. Host, L. Infante, S. Jha, Y. Jimenez-Teja, D. Kelson, O. Lahav, R. Lazkoz, D. Maoz, C. McCully, P. Melchior, M. Meneghetti, J. Merten, J. Moustakas, M. Nonino, B. Patel, E. Regös, J. Sayers, S. Seitz, and A. Van der Wel, *The Cluster Lensing and Supernova Survey with Hubble: An Overview*, ApJS **199** (Apr., 2012) 25, [arXiv:1106.3328].

[22] P. Rosati, I. Balestra, C. Grillo, A. Mercurio, M. Nonino, A. Biviano, M. Girardi, E. Vanzella, and Clash-VLT Team, *CLASH-VLT: A VIMOS Large Programme to Map the Dark Matter Mass Distribution in Galaxy Clusters and Probe Distant Lensed Galaxies*, The Messenger **158** (Dec., 2014) 48–53.

[23] G. A. Mamon, A. Biviano, and G. Boué, *MAMPOSSt: Modelling Anisotropy and Mass Profiles of Observed Spherical Systems - I. Gaussian 3D velocities*, MNRAS **429** (Mar., 2013) 3079–3098, [arXiv:1212.1455].

[24] J. F. Navarro, C. S. Frenk, and S. D. M. White, *A Universal Density Profile from Hierarchical Clustering*, ApJ **490** (Dec., 1997) 493–508, [astro-ph/9611107].

[25] B. Li, G.-B. Zhao, and K. Koyama, *Haloes and voids in f(R) gravity*, MNRAS **421** (Apr., 2012) 3481–3487, [arXiv:1111.2602].

[26] K. Umetsu, A. Zitrin, D. Gruen, J. Merten, M. Donahue, and M. Postman, *CLASH: Joint Analysis of Strong-lensing, Weak-lensing Shear, and Magnification Data for 20 Galaxy Clusters*, ApJ **821** (Apr., 2016) 116, [arXiv:1507.04385].

[27] V. Mukhanov, *Physical Foundations of Cosmology*. Mar., 2001.

[28] J. M. Bardeen, *Gauge-invariant cosmological perturbations*, Phys. Rev. D **22** (Oct., 1980) 1882–1905.

[29] L. Amendola, M. Kunz, M. Motta, I. D. Saltas, and I. Sawicki, *Observables and unobservables in dark energy cosmologies*, Phys. Rev. D **87** (Jan., 2013) 023501, [arXiv:1210.0439].

[30] A. de Felice, T. Kobayashi, and S. Tsujikawa, *Effective gravitational couplings for cosmological perturbations in the most general scalar-tensor theories with second-order field equations*, *Physics Letters B* **706** (Dec., 2011) 123–133, [arXiv:1108.4242].

[31] J. F. Navarro, C. S. Frenk, and S. D. M. White, *A Universal Density Profile from Hierarchical Clustering*, ApJ **490** (Dec., 1997) 493–+, [astro-ph/9].

[32] H. A. Buchdahl, *Non-linear Lagrangians and cosmological theory*, MNRAS **150** (1970) 1.

[33] M. Cataneo, D. Rapetti, L. Lombriser, and B. Li, *Cluster abundance in chameleon $f(R)$ gravity I: toward an accurate halo mass function prediction*, ArXiv e-prints (July, 2016) [arXiv:1607.08788].

[34] L. Pogosian and A. Silvestri, *Erratum: Pattern of growth in viable f(R) cosmologies [Phys. Rev. D 77, 023503 (2008)]*, Phys. Rev. D **81** (Feb., 2010) 049901.

[35] Y.-S. Song, W. Hu, and I. Sawicki, *Large scale structure of f(R) gravity*, Phys. Rev. D **75** (Feb., 2007) 044004, [astro-ph/0610532].

[36] H. Oyaizu, *Nonlinear evolution of f(R) cosmologies. I. Methodology*, Phys. Rev. D **78** (Dec., 2008) 123523, [arXiv:0807.2449].

[37] F. Schmidt, *Dynamical masses in modified gravity*, Phys. Rev. D **81** (May, 2010) 103002, [arXiv:1003.0409].

[38] G. A. Mamon and E. L. Łokas, *Dark matter in elliptical galaxies - II. Estimating the mass within the virial radius*, MNRAS **363** (Nov., 2005) 705–722, [astro-ph/0405491].

[39] M. Falco, S. H. Hansen, R. Wojtak, and G. A. Mamon, *Why does the Jeans Swindle work?*, MNRAS **431** (Apr., 2013) L6–L9, [arXiv:1210.3363].

[40] A. Biviano, P. Rosati, I. Balestra, A. Mercurio, M. Girardi, M. Nonino, C. Grillo, M. Scodeggio, D. Lemze, D. Kelson, K. Umetsu, M. Postman, A. Zitrin, O. Czoske, S. Ettori, A. Fritz, M. Lombardi, C. Maier, E. Medezinski, S. Mei, V. Presotto, V. Strazzullo, P. Tozzi, B. Ziegler, M. Annunziatella, M. Bartelmann, N. Benitez, L. Bradley, M. Brescia, T. Broadhurst, D. Coe, R. Demarco, M. Donahue, H. Ford, R. Gobat, G. Graves, A. Koekemoer, U. Kuchner, P. Melchior, M. Meneghetti, J. Merten, L. Moustakas, E. Munari, E. Regős, B. Sartoris, S. Seitz, and W. Zheng, *CLASH-VLT: The mass, velocity-anisotropy, and pseudo-phase-space density profiles of the z = 0.44 galaxy cluster MACS J1206.2-0847*, A&A **558** (Oct., 2013) A1, [arXiv:1307.5867].

[41] M. Girardi, A. Mercurio, I. Balestra, M. Nonino, A. Biviano, C. Grillo, P. Rosati, M. Annunziatella, R. Demarco, A. Fritz, R. Gobat, D. Lemze, V. Presotto, M. Scodeggio, P. Tozzi, G. Bartosch Caminha, M. Brescia, D. Coe, D. Kelson, A. Koekemoer, M. Lombardi, E. Medezinski, M. Postman, B. Sartoris, K. Umetsu, A. Zitrin, W. Boschin, O. Czoske, G. De Lucia, U. Kuchner, C. Maier, M. Meneghetti, P. Monaco, A. Monna, E. Munari, S. Seitz, M. Verdugo, and B. Ziegler, *CLASH-VLT: Substructure in the galaxy cluster MACS J1206.2-0847 from kinematics of galaxy populations*, A&A **579** (July, 2015) A4, [arXiv:1503.05607].

[42] D. Lemze, M. Postman, S. Genel, H. C. Ford, I. Balestra, M. Donahue, D. Kelson, M. Nonino, A. Mercurio, A. Biviano, P. Rosati, K. Umetsu, D. Sand, A. Koekemoer, M. Meneghetti, P. Melchior, A. B. Newman, W. A. Bhatti, G. M. Voit, E. Medezinski, A. Zitrin, W. Zheng, T. Broadhurst, M. Bartelmann, N. Benitez, R. Bouwens, L. Bradley, D. Coe, G. Graves, C. Grillo, L. Infante, Y. Jimenez-Teja, S. Jouvel, O. Lahav, D. Maoz, J. Merten, A. Molino, J. Moustakas, L. Moustakas, S. Ogaz, M. Scodeggio, and S. Seitz, *The Contribution of Halos with Different Mass Ratios to the Overall Growth of Cluster-sized Halos*, ApJ **776** (Oct., 2013) 91, [`arXiv:1308.1675`].

[43] K. Umetsu, E. Medezinski, M. Nonino, J. Merten, A. Zitrin, A. Molino, C. Grillo, M. Carrasco, M. Donahue, A. Mahdavi, D. Coe, M. Postman, A. Koekemoer, N. Czakon, J. Sayers, T. Mroczkowski, S. Golwala, P. M. Koch, K.-Y. Lin, S. M. Molnar, P. Rosati, I. Balestra, A. Mercurio, M. Scodeggio, A. Biviano, T. Anguita, L. Infante, G. Seidel, I. Sendra, S. Jouvel, O. Host, D. Lemze, T. Broadhurst, M. Meneghetti, L. Moustakas, M. Bartelmann, N. Benítez, R. Bouwens, L. Bradley, H. Ford, Y. Jiménez-Teja, D. Kelson, O. Lahav, P. Melchior, J. Moustakas, S. Ogaz, S. Seitz, and W. Zheng, *CLASH: Mass Distribution in and around MACS J1206.2-0847 from a Full Cluster Lensing Analysis*, ApJ **755** (Aug., 2012) 56, [`arXiv:1204.3630`].

[44] O. Tiret, F. Combes, G. W. Angus, B. Famaey, and H. S. Zhao, *Velocity dispersion around ellipticals in MOND*, A&A **476** (Dec., 2007) L1–L4, [`arXiv:0710.4070`].

[45] G. A. Mamon, A. Biviano, and G. Murante, *The universal distribution of halo interlopers in projected phase space. Bias in galaxy cluster concentration and velocity anisotropy?*, A&A **520** (Sept., 2010) A30, [`arXiv:1003.0033`].

[46] J. Einasto, *On the Construction of a Composite Model for the Galaxy and on the Determination of the System of Galactic Parameters*, Trudy Astrofizicheskogo Instituta Alma-Ata **5** (1965) 87–100.

[47] L. Hernquist, *An analytical model for spherical galaxies and bulges*, ApJ **356** (June, 1990) 359–364.

[48] A. Burkert, *The Structure of Dark Matter Halos in Dwarf Galaxies*, ApJ **447** (July, 1995) L25, [`astro-ph/9504041`].

[49] M. J. Geller, A. Diaferio, and M. J. Kurtz, *The Mass Profile of the Coma Galaxy Cluster*, ApJ **517** (May, 1999) L23–L26, [`astro-ph/9903305`].

[50] A. Zitrin, T. Broadhurst, R. Barkana, Y. Rephaeli, and N. Benítez, *Strong-lensing analysis of a complete sample of 12 MACS clusters at z > 0.5: mass models and Einstein radii*, MNRAS **410** (Jan., 2011) 1939–1956, [`arXiv:1002.0521`].

[51] J. Merten, M. Meneghetti, M. Postman, K. Umetsu, A. Zitrin, E. Medezinski, M. Nonino, A. Koekemoer, P. Melchior, D. Gruen, L. A. Moustakas, M. Bartelmann, O. Host, M. Donahue, D. Coe, A. Molino, S. Jouvel, A. Monna, S. Seitz, N. Czakon, D. Lemze, J. Sayers, I. Balestra, P. Rosati, N. Benítez, A. Biviano, R. Bouwens, L. Bradley, T. Broadhurst, M. Carrasco, H. Ford, C. Grillo, L. Infante, D. Kelson, O. Lahav, R. Massey, J. Moustakas, E. Rasia, J. Rhodes, J. Vega, and W. Zheng, *CLASH: The Concentration-Mass Relation of Galaxy Clusters*, ApJ **806** (June, 2015) 4, [`arXiv:1404.1376`].

[52] K. Umetsu, E. Medezinski, M. Nonino, J. Merten, M. Postman, M. Meneghetti, M. Donahue, N. Czakon, A. Molino, S. Seitz, D. Gruen, D. Lemze, I. Balestra, N. Benítez, A. Biviano, T. Broadhurst, H. Ford, C. Grillo, A. Koekemoer, P. Melchior, A. Mercurio, J. Moustakas, P. Rosati, and A. Zitrin, *CLASH: Weak-lensing Shear-and-magnification Analysis of 20 Galaxy Clusters*, ApJ **795** (Nov., 2014) 163, [`arXiv:1404.1375`].

[53] A. Zitrin, A. Fabris, J. Merten, P. Melchior, M. Meneghetti, A. Koekemoer, D. Coe, M. Maturi, M. Bartelmann, M. Postman, K. Umetsu, G. Seidel, I. Sendra, T. Broadhurst, I. Balestra, A. Biviano, C. Grillo, A. Mercurio, M. Nonino, P. Rosati, L. Bradley, M. Carrasco,

M. Donahue, H. Ford, B. L. Frye, and J. Moustakas, *Hubble Space Telescope Combined Strong and Weak Lensing Analysis of the CLASH Sample: Mass and Magnification Models and Systematic Uncertainties*, ApJ **801** (Mar., 2015) 44, [`arXiv:1411.1414`].

[54] G. O. Abell, H. G. Corwin, Jr., and R. P. Olowin, *A catalog of rich clusters of galaxies*, ApJS **70** (May, 1989) 1–138.

[55] A. Monna, S. Seitz, N. Greisel, T. Eichner, N. Drory, M. Postman, A. Zitrin, D. Coe, A. Halkola, S. H. Suyu, C. Grillo, P. Rosati, D. Lemze, I. Balestra, J. Snigula, L. Bradley, K. Umetsu, A. Koekemoer, U. Kuchner, L. Moustakas, M. Bartelmann, N. Benítez, R. Bouwens, T. Broadhurst, M. Donahue, H. Ford, O. Host, L. Infante, Y. Jimenez-Teja, S. Jouvel, D. Kelson, O. Lahav, E. Medezinski, P. Melchior, M. Meneghetti, J. Merten, A. Molino, J. Moustakas, M. Nonino, and W. Zheng, *CLASH: $z \sim 6$ young galaxy candidate quintuply lensed by the frontier field cluster RXC J2248.7-4431*, MNRAS **438** (Feb., 2014) 1417–1434, [`arXiv:1308.6280`].

[56] T. L. Johnson, K. Sharon, M. B. Bayliss, M. D. Gladders, D. Coe, and H. Ebeling, *Lens Models and Magnification Maps of the Six Hubble Frontier Fields Clusters*, ApJ **797** (Dec., 2014) 48, [`arXiv:1405.0222`].

[57] J. Richard, M. Jauzac, M. Limousin, E. Jullo, B. Clément, H. Ebeling, J.-P. Kneib, H. Atek, P. Natarajan, E. Egami, R. Livermore, and R. Bower, *Mass and magnification maps for the Hubble Space Telescope Frontier Fields clusters: implications for high-redshift studies*, MNRAS **444** (Oct., 2014) 268–289, [`arXiv:1405.3303`].

[58] G. B. Caminha, C. Grillo, P. Rosati, I. Balestra, W. Karman, M. Lombardi, A. Mercurio, M. Nonino, P. Tozzi, A. Zitrin, A. Biviano, M. Girardi, A. M. Koekemoer, P. Melchior, M. Meneghetti, E. Munari, S. H. Suyu, K. Umetsu, M. Annunziatella, S. Borgani, T. Broadhurst, K. I. Caputi, D. Coe, C. Delgado-Correal, S. Ettori, A. Fritz, B. Frye, R. Gobat, C. Maier, A. Monna, M. Postman, B. Sartoris, S. Seitz, E. Vanzella, and B. Ziegler, *CLASH-VLT: A highly precise strong lensing model of the galaxy cluster RXC J2248.7-4431 (Abell S1063) and prospects for cosmography*, A&A **587** (Mar., 2016) A80, [`arXiv:1512.04555`].

[59] D. Gruen, F. Brimioulle, S. Seitz, C.-H. Lee, J. Young, J. Koppenhoefer, T. Eichner, A. Riffeser, V. Vikram, T. Weidinger, and A. Zenteno, *Weak lensing analysis of RXC J2248.7-4431*, MNRAS **432** (June, 2013) 1455–1467, [`arXiv:1304.0764`].

[60] J. Merten, M. Meneghetti, M. Postman, K. Umetsu, A. Zitrin, E. Medezinski, M. Nonino, A. Koekemoer, P. Melchior, D. Gruen, L. A. Moustakas, M. Bartelmann, O. Host, M. Donahue, D. Coe, A. Molino, S. Jouvel, A. Monna, S. Seitz, N. Czakon, D. Lemze, J. Sayers, I. Balestra, P. Rosati, N. Benítez, A. Biviano, R. Bouwens, L. Bradley, T. Broadhurst, M. Carrasco, H. Ford, C. Grillo, L. Infante, D. Kelson, O. Lahav, R. Massey, J. Moustakas, E. Rasia, J. Rhodes, J. Vega, and W. Zheng, *CLASH: The Concentration-Mass Relation of Galaxy Clusters*, ApJ **806** (June, 2015) 4, [`arXiv:1404.1376`].

[61] P. Melchior, E. Suchyta, E. Huff, M. Hirsch, T. Kacprzak, E. Rykoff, D. Gruen, R. Armstrong, D. Bacon, K. Bechtol, G. M. Bernstein, S. Bridle, J. Clampitt, K. Honscheid, B. Jain, S. Jouvel, E. Krause, H. Lin, N. MacCrann, K. Patton, A. Plazas, B. Rowe, V. Vikram, H. Wilcox, J. Young, J. Zuntz, T. Abbott, F. B. Abdalla, S. S. Allam, M. Banerji, J. P. Bernstein, R. A. Bernstein, E. Bertin, E. Buckley-Geer, D. L. Burke, F. J. Castander, L. N. da Costa, C. E. Cunha, D. L. Depoy, S. Desai, H. T. Diehl, P. Doel, J. Estrada, A. E. Evrard, A. F. Neto, E. Fernandez, D. A. Finley, B. Flaugher, J. A. Frieman, E. Gaztanaga, D. Gerdes, R. A. Gruendl, G. R. Gutierrez, M. Jarvis, I. Karliner, S. Kent, K. Kuehn, N. Kuropatkin, O. Lahav, M. A. G. Maia, M. Makler, J. Marriner, J. L. Marshall, K. W. Merritt, C. J. Miller, R. Miquel, J. Mohr, E. Neilsen, R. C. Nichol, B. D. Nord, K. Reil, N. A. Roe, A. Roodman, M. Sako, E. Sanchez, B. X. Santiago, R. Schindler, M. Schubnell, I. Sevilla-Noarbe, E. Sheldon, C. Smith, M. Soares-Santos, M. E. C. Swanson, A. J. Sypniewski, G. Tarle, J. Thaler,

D. Thomas, D. L. Tucker, A. Walker, R. Wechsler, J. Weller, and W. Wester, *Mass and galaxy distributions of four massive galaxy clusters from Dark Energy Survey Science Verification data*, MNRAS **449** (May, 2015) 2219–2238, [arXiv:1405.4285].

[62] P. L. Gómez, L. E. Valkonen, A. K. Romer, E. Lloyd-Davies, T. Verdugo, C. M. Cantalupo, M. D. Daub, J. H. Goldstein, C. L. Kuo, A. E. Lange, M. Lueker, W. L. Holzapfel, J. B. Peterson, J. Ruhl, M. C. Runyan, C. L. Reichardt, and K. Sabirli, *Optical and X-Ray Observations of the Merging Cluster AS1063*, AJ **144** (Sept., 2012) 79.

[63] A. Biviano and P. Salucci, *The radial profiles of the different mass components in galaxy clusters*, A&A **452** (June, 2006) 75–81, [astro-ph/0511309].

[64] M. Bartelmann, *Arcs from a universal dark-matter halo profile.*, A&A **313** (Sept., 1996) 697–702, [astro-ph/9602053].

[65] T. C. Beers, K. Flynn, and K. Gebhardt, *Measures of location and scale for velocities in clusters of galaxies - A robust approach*, AJ **100** (July, 1990) 32–46.

[66] L. Lombriser, K. Koyama, G.-B. Zhao, and B. Li, *Chameleon f(R) gravity in the virialized cluster*, Phys. Rev. D **85** (June, 2012) 124054, [arXiv:1203.5125].

[67] B. Jain, V. Vikram, and J. Sakstein, *Astrophysical Tests of Modified Gravity: Constraints from Distance Indicators in the Nearby Universe*, ApJ **779** (Dec., 2013) 39, [arXiv:1204.6044].

[68] F. Schmidt, M. Lima, H. Oyaizu, and W. Hu, *Nonlinear evolution of f(R) cosmologies. III. Halo statistics*, Phys. Rev. D **79** (Apr., 2009) 083518–+, [arXiv:0812.0545].

[69] L. Xu, *Constraints on f(r) gravity through the redshift space distortion*, Phys. Rev. D **91** (Mar, 2015) 063008.

[70] H. Kim, *Brans-Dicke theory as a unified model for dark matter-dark energy*, MNRAS **364** (Dec., 2005) 813–822, [astro-ph/0408577].